ADVANCED MATERIALS TECHNOLOGIES
www.advmattechnol.de

Recent Developments in Halide Perovskite Nanocrystals for Indirect X-ray Detection

*Olexiy Balitskii, Mykhailo Sytnyk, and Wolfgang Heiss**

Metal halide perovskites are revolutionizing X-ray detection through a combination of low cost, solution processing, favorable optoelectronic properties, and high stopping power for high-energy ionizing radiation. While perovskite single crystals and polycrystalline wafers are considered direct X-ray converters, most medical X-ray applications are based on scintillators that shift high-energy radiation into the visible. Several materials are on the market, but demonstrations based on $CsPbBr_3$ nanocrystals, possibly embedded in a matrix material or combined with organic molecules as luminescent species, highlight their competitiveness with established scintillators in terms of radioluminescence yield and transient behavior. Major hurdles that perovskite nanocrystal scintillators must overcome are environmental stability and toxicity. While there are still few examples of high-performance lead-free perovskite nanocrystal scintillators, microcrystalline perovskites are emerging with promising properties, reduced toxicity, and significant Stokes shifts to avoid reabsorption of emission in thick films. Thus, the near future of perovskite nanocrystal scintillator materials will primarily be the adoption of recipes for materials with proven properties in microcrystalline form. The nanocrystal colloidal solutions will facilitate the large-scale printing of homogeneous and scattering-free films to obtain high contrast and spatial resolution X-ray images by scintillation.

1. Introduction

Organic-inorganic and all-inorganic halide perovskites (HPs) have recently been intensively studied for their diverse applications in monochrome and white light-emitting diodes,[1a] in photodiodes and transistors,[1b] for water-splitting,[1c] energy storage,[1d] and as efficient absorbers in solar photovoltaic cells.[1e,f] Different cations and anions can be incorporated during the fabrication of HPs, and also exchanged post-synthetically,[2a] to widely tune the perovskite bandgaps, carrier densities, and mobility values. Tuning their composition allows the design of the luminescence, transport, and catalytic properties of HPs and related structures.[2b,c] Consisting of heavy cations (caesium, lead, copper, bismuth) and halide anions, HPs are also widely studied as direct X-ray detectors and down-conversion-based scintillating imagers.[3a] The latter would benefit from high exciton binding energies and near-unity photoluminescence quantum yields but also suffer from reabsorption losses.[3b]

A pressing need today is the detection of X- and γ-ray photons of different energies. For example, point-of-care facilities operate a variety of X-ray sources, specifically from 150 keV for whole-body scans down to 50 and 20 keV, which is implied in local imaging in dentistry and mammography, respectively.[4a] The former high-energy medical radiography deficiencies in some common cases (e.g., obesity, in-bone scans, etc.) require either increased radiation doses[4b] or enhanced penetration capability, given by shorter wavelength sources.[4c]

O. Balitskii, W. Heiss
Faculty of Engineering
Department of Material Science
Materials for Electronics and Energy Technology (i-MEET)
Friedrich-Alexander-University Erlangen-Nuremberg (FAU)
Martensstraße 7, 91058 Erlangen, Germany
E-mail: wolfgang.heiss@fau.de

The ORCID identification number(s) for the author(s) of this article can be found under https://doi.org/10.1002/admt.202400150

DOI: 10.1002/admt.202400150

O. Balitskii, W. Heiss
Faculty of Engineering
Department of Material Science
Materials for Electronics and Energy Technology (i-MEET)
Friedrich-Alexander-University Erlangen-Nuremberg (FAU)
Energy Campus Nürnberg
Fürtherstraße 250, 90429 Nürnberg, Germany

M. Sytnyk
Department of High Throughput Methods in Photovoltaics
Helmholtz-Institute Erlangen-Nürnberg (HI ERN)
91058 Erlangen, Germany

The industrial requirements (e.g., homeland security and cargo radiography) in active and passive screening, inspection, and identification cover broader radiation energies, typically up to 10 MeV.[4d] Systematic studies on scintillators have selected those materials that offer a balance between high X-ray cross-sections, photoluminescence (PL) with near-unity quantum yields (PLQY) and decent Stokes shifts, improved radiation resistance and environmental stability, and linear response as a function of absorbed radiation dose. Organic scintillators offer various Förster and radiative energy transfer processes, from aromatic matrices as primary absorbers to fluorophore dye molecules as wave-shifters, separating absorption and emission between different organic components.[5a] Commercial organic scintillators are competitive as soft X-ray detectors due to high light yields, good spectral matching of radioluminescence (RL) spectra to conventional Si detectors, and negligible reabsorption, although they are outperformed in stopping power by high Z inorganic scintillators.[5b] Detection materials for harder X-rays and γ require higher stopping powers than organic scintillators to keep scintillator thicknesses sufficiently small. The solution to broaden the applicability of organic scintillators is to sensitize them by adding high-Z materials in the form of heavy organometallic complexes or inorganic nanoparticles, but this adds complexity to the device assembly and requires careful design of the energy transfer pathways.[5a] The best performing but most expensive are single crystal (SC) detectors made from pure or activated tungstates, garnets, perovskites, and silicates.[5c–e] These are also advantageous for imaging high-momentum fluences of neutrons and alpha particles due to their enhanced radiation resistance.

Historically, scintillating oxide materials were introduced simultaneously with the invention of X-rays by Roentgen.[6a,b] The natural calcium scheelite minerals used for the pioneering X-ray detectors in the 19th century were tungstates. Tungstates, mostly in the form of variously processed CdWO4 materials, are still routinely used in X-ray imaging and computed tomography.[6c] Cost, toxicity, high processing temperature, and poor scalability of the SC covalent oxide growth techniques are the major drawbacks preventing further expansion of their applications. Conversely, ionic bonding in HP facilitates low-temperature solution processes for the development of single, micro (MC), and nanocrystalline (NC) devices. Colloidal nanocrystals can be used to formulate stable inks suitable for printing and for easy, high-throughput, large-scale deposition of scintillators with desired geometries on various substrates, including imaging devices such as a-Si photodetector pixel arrays. In the latter case, the deposition must be performed at low temperatures to avoid damage to the detectors. Recently, SC HP direct and indirect detectors have made tremendous progress due to feasible solution growth and high sensitivity to various types of ionizing radiation.[7a–d]

Although HP NC assemblies for direct detection have been reviewed,[7e–g] the challenges of applicability, shortcomings, and perspectives of HP nanocrystals in indirect detectors have not been summarized. Currently in medical diagnostics, except in mammography, exclusively scintillator-based X-ray detectors are used for imaging. The reason for this preference is, that scintillators are applied in combination with optimized photodiode arrays that are used for the conversion of the scintillator radiation into electrical signals. These diode arrays are based on standard semiconductor technologies, providing photodiodes with extremely low dark currents and thus extremely low noise. X-ray direct converting detectors, even though having high sensitivity, either provide too much dark current as is the case for practically all photoconductive perovskite materials, or are weak absorbers for X-ray radiation, as the amorphous Selenium applied in mammography. In photoluminescence quantum yield the colloidal nanocrystals, when properly passivated, can outperform the single-crystal materials, so they are ideally suited for scintillator applications. Thus, this paper reviews the recent advances in the synthesis of halide perovskite NCs, describes the mechanisms of their electronic structure control, and focuses on the state-of-the-art approaches in down-conversion of high-energy photons, as is desired in scintillators applied for X-ray imaging devices. The nanocrystal-based scintillator performances are discussed and a critical view on parameter comparison is provided, finally suggesting that standards should be established for the characterization of scintillators to provide a useful guide for potential applications in medicine, X-ray spectroscopy, or security inspection.

2. Nature of Indirect High Energy Photon Detection

High-energy radiation detection is generally based on strategies of temporally and spatially resolved tracking of ionization events that have occurred. Traditional high-energy Geiger detectors are based on ionized gas discharges. Solid-state detectors are much denser than gases, overcoming the efficiency and accuracy of gas detectors. Semiconductor detectors allow the fabrication of large arrays with improved spatial resolution, are more sensitive to longer wavelengths of radiation due to lower ionization energies, and have faster readouts and shorter dead times. In semiconductors, inner ionization of the atoms occurs when high-energy photons are either completely absorbed or inelastically scattered. Here, "inner" means that the photo-excited electron is removed from an atom in the semiconductor, but is not removed to the vacuum after excitation; instead, it remains within the bulk of the semiconductor. The inner photoelectron excitation and its effect on the free carrier concentration are sketched in **Figure 1a**). After excitation by photon absorption, inner electrons are highly excited and released from their parent atom, creating deep nuclear holes (Figure 1a). Subsequently, electrons from an outer shell fill the deep holes by Auger recombination or by emission of secondary electromagnetic radiation. This leads to a multiplication of holes in the higher levels of the nucleus and gradually also to holes in the valence band of the bulk material. On the other hand, the energy dissipation of the high-energy electrons is associated with the excitation of further electron-hole pairs due to inelastic scattering by electron-phonon interactions, causing an increase in the lattice temperature. Thermalized electrons and holes localize in conduction and valence bands and either form free excitons or can be trapped by luminescence centers in the scintillator material, forming bound excitons that contribute to photon emission at reduced energies. Alternatively, the electron-hole pairs can be trapped for radiative recombination by lattice point defects such as cation and anion vacancies, either intrinsic or radiation or thermal induced. Other defects include aliovalent ions and bulkier defects such as dislocations and grain boundaries. These defects eventually lead to trap states that favor

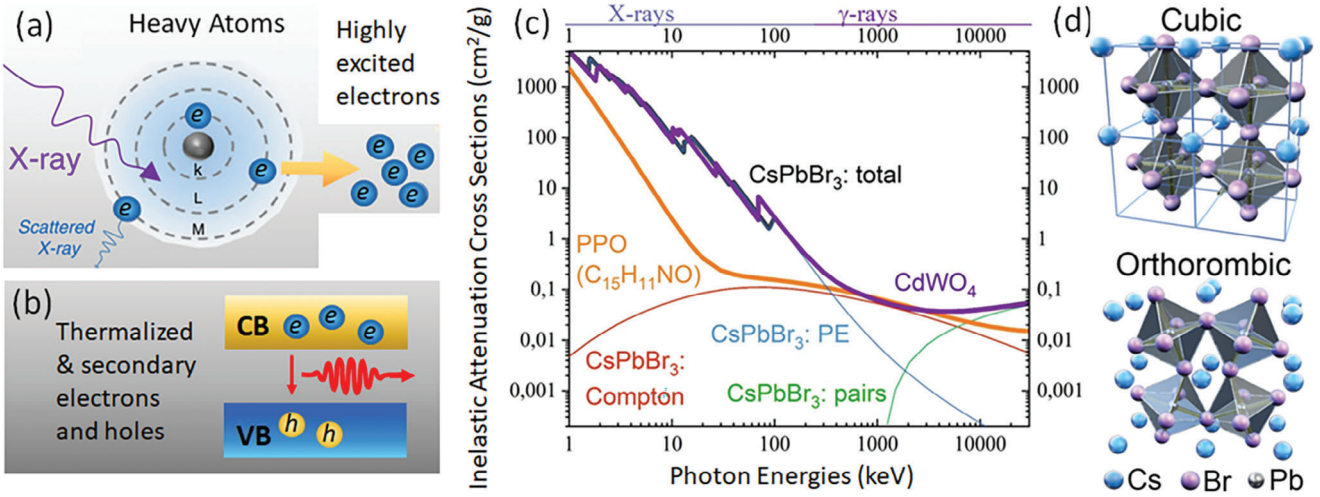

Figure 1. a,b): Sketch of the inner photoelectric effect and the generation of multiple excitons creating radioluminescence (Adapted with permission.[8a] Copyright 2021, Springer Nature); c) Comparison of inelastic attenuation cross-sections for $CsPbBr_3$, cadmium wolframate, and diphenyloxazole (PPO) scintillators and contributions of the photoelectric effect, the Compton scattering and pair production to the total cross-section of $CsPbBr_3$ calculated using XCOM database.[8b] d) Crystal structure of cesium lead bromide exhibiting the most common cubic pm3m (top), and orthorhombic pnma $CsPbBr_3$ (bottom) phases.

nonradiative recombination of the excitons, reducing the efficiency and degrading the detection limit of the scintillators. The defects can accumulate over the lifetime of the detector, especially for high-energy photon detection devices. The carriers trapped in the defect sites are also responsible for a delay of the luminescence, often seen as an unwanted afterglow, which reduces the temporal and spatial resolution of the scintillator detection. The chosen detector processing must avoid defects through crystal quality control and surface passivation during and after the syntheses. While the internal photoelectric effect (PE) dominates the inelastic attenuation cross section at X-ray energies below ≈300 keV, the Compton effect becomes relevant at higher energies (Figure 1b).

The Compton effect is an inelastic scattering process in which the incident photon deposits only part of its energy in the scattering atom, resulting in the excitation of electrons. For incident γ rays whose energies exceed the threshold of 2 free electron masses (1.02 MeV), pair production will be the dominant inelastic scattering mechanism. This process also produces electron holes, either directly or indirectly via positron annihilation. The absorption cross-section in the energy region where the internal photoelectric effect dominates is highest for heavy elements with high order number Z. Thus, lead halide perovskites are ideally suited for X-ray detection in these regions because the incorporated Pb represents the nuclei with the highest Z value, which is still non-radioactive. The next element in the periodic table of elements is Bi, which would still be acceptable due to its very slow radioactive decay, but Bi-based perovskites exhibit much lower photoluminescence efficiencies than lead halide-based ones. In the region where pair production in a nuclear field dominates, the lead halide perovskites exhibit essentially the same small attenuation coefficient as many other materials. In this region, the only advantage of lead-halide perovskites may be their self-healing property, discussed below, which allows them to compensate for performance losses due to radiation damage. In contrast to halide perovskite single crystals, which exhibit slow photoluminescence decay with components in the ms lifetime range, lead-halide NC assemblies typically exhibit short decay times in the ns range or faster.[9] The applications of scintillating detectors require either rather high radiative recombination rates of excitons in the UV-VIS (c.a. 10^9–10^{12} s^{-1}), which competes with nonradiative recombination, which can be assisted by trap states. The relative efficiency quantifies the ratio of radiative to non-radiative recombination,[10] which can be read as the energy of the emitted photons ($E_{em} \cdot N_{ph}$) versus the energy of the absorbed X-rays or γ-rays (E_{abs}):

$$\eta = \frac{E_{em} \cdot N_{ph}}{E_{abs}} \quad (1)$$

Even for the best detector, the relative efficiency rarely exceeds 20% due to nonradiative and radiative losses (e.g., secondary photons, Compton scattered photons). For practical use, it is more convenient to omit the energy of the emitted photons in Equation (1) and to express the detector efficiency as the light yield (number of emitted photons per MeV of an incident photon). Important for this number is also the absorption coefficient for high-energy electromagnetic radiation, which can be roughly expressed as

$$\alpha = \frac{\rho \cdot Z^4}{A \cdot E_{abs}^3} \quad (2)$$

where ρ is the material density, Z and A are the averaged atomic number and mass, respectively. One should choose denser materials (obviously with higher average atomic numbers) to improve detector performance for as thin films as possible. Such materials are also advantageous in terms of radiation resistance since their atoms can scatter higher energy (higher momentum) photons without in-lattice displacements. The power to the cube

dependence of the photon energy in the denominator of Equation (2) indicates the toughness in the precise detection of γ rays whose primary scattering mechanism is electron-positron production that rapidly annihilates into secondary γ quants.

3. Crystal Structure, Electronic Properties of HP NCs, and Approaches to their Syntheses

Obviously, the common feature of the materials classified as "perovskites" is their relationship to a particular lattice structure. Therefore, let us first present the crystal structure of the perovskites, which in fact goes back to that of calcium titanate, but is discussed here for lead bromide perovskite (Figure 1d,e). It shows the most common cubic Pm3m phase at room temperature. The lattice consists of lead bromide tetraanions $[PbBr_6]^{4-}$ surrounding cesium or isovalent organic monocations (shown in blue in Figure 1d), which balance the net crystal charge. Variation of the structural geometry (Figure 1e) of lead halide tetraanions (i.e., their displacement, stretching, or stretching) results in phase transitions to various pseudocubic (tetragonal, orthorhombic) lattices in which the $[PbBr_6]^{4-}$ ions deviate from the ideal octahedral geometry. This occurs in the dynamically disordered phases of cesium lead halides consisting of bulkier iodine anions or isovalently substituted lead. For typical short alkylamine (MA, FA) cations, the NCs usually retain their original stable cubic structure. The double (sesqui-) perovskites (e.g., Cs_4PbBr_6, Cs_3PbBr_5) have a stoichiometric imbalance of their monovalent cations. These are periodically displaced from primarily linearly aligned positions (Figure 1), but open the possibility of more diverse cation exchanges. Due to the ideal alignment of $[PbBr_6]_{4-}$ and the monocations A^+ therein, the hybridization in halide perovskites obeying a sum formula of $APbX_3$ is due to an overlap of p-orbitals of the halides with s- and p-orbitals of lead. Quantum confinement effects of the optical properties in HPs are observed when the dimensions are reduced from bulk material to NCs. On the other hand, unaligned $[PbBr_6]^{4-}$ in A_4PbX_6 act as single radiation centers and are classified as 0D semiconductors or 0D "perovskites", inheriting electronic properties of lead halide precursors. "Bulk" $APbX_3$ single and nanocrystals have broader absorption spectra and their PL is red-shifted with respect to their lower dimensional A_3BX_5 and A_4BX_6 counterparts. The singlet-triplet splitting in lead halide perovskites (LHP) results in a tiny Stokes shift (about tens of meV). This is already observed in concentrated solutions and even more so in densely packed NC films, which are less luminescent than their diluted counterparts. This shortcoming is most pronounced in the bright triplet materials, and applications in scintillating films typically require size, shape, or dopant control to increase the Stokes shift or the use of additional dyes coupled to the HP NCs as emitters. The first HP nanocrystals were accidentally obtained by attempting to grow lead-activated cesium halide SC scintillators from metal halide melts using the Bridgman technique.[11a] Instead of forming substitutional point defects as in activated sodium halides, the intended high-temperature CsCl:Pb growth resulted in the nucleation of $CsPbCl_3$ NCs exhibiting PL with near-unity quantum yield and subnanosecond decay times. Subsequently, this growth process was improved to control the size, anion composition, and optical properties of the NCs via tunable annealing procedures,[11b] sorting of anion sublattices[11c] and host matrices,[11d] and elucidation of the nucleation of HP and 0D HP NCs during thin film deposition.[11e] The major drawback of such NCs has been that they are irreversibly embedded in SCs or thin-film matrices during the preparation stage, limiting further NC processing. The Kovalenko group has overcome this drawback by introducing a solution-processed approach. Their high-quality, narrow, size-distributed lead HP NCs of cubic shape were synthesized via a conventional colloidal hot injection route in a high-boiling point coordinating solvent (octadecene) under an inert gas atmosphere,[12a] where a cesium oleate was injected into a dissolved lead halide precursor enriched with stabilizing agents, namely oleylamine and oleic acid. As mentioned above, HPs are predominantly ionic bonds, so the NC sizes were mainly controlled by the reaction temperature, with prolonged reaction time being responsible for the growth of bulkier nanowires and nanoplatelets.[12b] The anion lattice composition can be set at the synthesis stage or changed post-synthetically by rapid mutual anion exchange.[12c,d] The lead HP NCs chemistry includes melt quenching, low-temperature "one-pot" syntheses, templated syntheses, solvo-(aqua-) thermal procedures, with implemented feasible precursors and surfactants. Later, the Konstantatos group introduced a room-temperature coprecipitation procedure in polar solvents.[13c] A subsequent post-synthetic NC surface functionalization in nonpolar media allowed us to achieve near-unity PL by selecting stronger binding ligands. Due to the ease of substitution of cesium for alkylamine ions in the perovskite lattice, specific add-on spacers of bulkier butyl or octyl ammonium can be added during SC growth. They break the interlayer ionic bonds and enable top-down approaches (e.g., tape-assisted mechanical exfoliation) for the fabrication of platelet-shaped NCs with excellent PLQY values and fast PL decays.[13d]

By using oleic acid species as ligands, surface functionalization was achieved in the pioneering work of L. Protesescu et al.[12a] and has been extensively applied by others as well.[14a] The ligand species are mainly chosen to provide improved luminescence properties, i.e., to suppress surface recombination and thermal quenching,[14b] for scintillator purposes where short ligands with low electrical resistance are not urgently needed. Among them, phosphonic complexes show better surface passivation, similar to what was observed for cadmium chalcogenide NCs.[14c] Later, specific metal-organic frameworks based on chromium and zinc were shown to tune the ultrafast scintillating properties of $CsPbBrCl_2$ NCs.[14d] While lead-containing perovskites show record performances not only in solar cells but also in colloidal nanocrystals, their use is limited due to their toxicity. Thus, there are many efforts to replace lead with other metals, in the best case by divalent ones. A prime candidate here is tin. Tin-based HP NCs were synthesized in Ref. [15a] by introducing trioctylphosphine as tin reducing agent. Extensive studies of tin-based HP NCs revealed luminescence properties inferior to those of lead-based HPs, combined with lower environmental stability.[15b] Tin-based perovskites are notoriously unstable because thermodynamically, Sn favors oxidation from (+2) to (+4), which destroys the metal halide tetraanion $[SnX_6]^{4-}$ that is the fundamental feature within perovskite semiconductors. Similar drawbacks, such as low luminescence, have been observed for bismuth HP NCs.[15c]

Antimony and europium-based perovskite NCs are more complicated to synthesize and require advanced surfactant chemistry

to prevent rapid degradation of the NCs PL.[15d] Naturally, metals with a native oxidation state of +3 and higher can only be involved in double perovskite configurations.[15e] These double perovskites, namely Cs_2ABX_6 (A represents a monovalent ion such as Na, K, Ag, and B represents a trivalent cation, X represents the halide), have recently emerged as materials with PLQY values close to untity. The reason may be that different cations have favorable coordination with A^+ and B^{3+} sites. These double HP ($Cs_2Ag_xNa_{1-x}InCl_6$, $Cs_2Ag_xNa_{1-x}BiCl_6$, $Cs_2Ag_xNa_{1-x}SbCl_6$, $Cs_2Ag_xNa_{1-x}YCl_6$, etc.) exhibit bandgap energies that are widely tunable by alloying with A+ alkali cations. The alkali cation-alloyed HPs either exhibit indirect band gaps or their optical transitions are forbidden at their direct band gaps.[15f–j] However, these forbidden transitions are broken by small traces of ns^2 B^{3+} ions doping (e.g., In/Bi, In/Sb, Y/Sb, Bi/Sb),[15f–j] stimulating broad and fast self-trapped exciton (STE) emission with near unity efficiencies. To increase the Stokes shift, double HP NCs can be doped with trivalent lanthanide cations. Alternatively, lanthanides are introduced as intrinsic ions at the B^{3+} sites.[15k–n] In both cases, high PLQY can be achieved, but the emission is significantly red-shifted. As a disadvantage, the lanthanide emission suffers from a slow decay time on the scale of 1–10 ms. Nevertheless, nanocrystals of interest for scintillator applications, mainly lead halide perovskites, have been investigated and reported in the literature.

4. Scintillating Detectors Assembled from Lead-Halide-Perovskite Nanocrystals

4.1. Beneficial Lead Halide Nanocrystal Materials

There is a limited number of lead-containing HP NCs due to a limit on possible ion combinations. The limitation is summarized by the Goldschmidt tolerance factor, which predicts size ranges for possible combinations of cations to form stable 3D HP compositions.[16] This limitation also limits the possibility of increasing the X-ray mass stopping power by introducing larger ions with higher Z-numbers. Thus, strategies to improve the scintillating properties of NCs focus on their electronic modifications, i.e., defect and surface control, increasing the Stokes shift and PLQY values, and eliminating slower components in the luminescence decays. The control of cesium vacancies, for example, is a crucial factor in obtaining a short PL decay,[17a] which is advantageous to avoid the long afterglow of X-ray detectors. Maddalena et al. carried out a preliminary study on the potential efficiency of HP NCs with regard to their application in scintillating detectors.[17b] The estimated luminescence efficiencies for Cu X-rays suggest $CsPbBr_3$ as a prime HP material for scintillator research due to its high conversion yield of ≈24 000 photons MeV^{-1}. Other luminescent HP NCs in the same family (e.g., $FAPbBr_3$ or $CsPbI_3$) are less efficient and provide light yields of ≈5 500 photons MeV^{-1}, although $CsPbI_3$ has a higher X-ray stopping power than the bromide. A lower light yield excludes many NCs based on 3-D perovskite materials compared to $CsPbBr_3$, although such NCs may have similar or even better afterglow characteristics. Their low light yield is related to thermal quenching of the luminescence by nonradiative recombination or to a tiny Stokes shift causing reabsorption losses, as is explicitly the case in $FAPbBr_3$ NC films.[17b]

4.2. $CsPbBr_3$ Nanocrystal Scintillation Performance in Solutions

X-ray detection using scintillating HP NCs usually starts by testing them in colloidal solutions. Zhang et al. prepared by co-precipitation $CsPbBr_3$ nanosheets exhibiting strong radioluminescence response.[18a] A concentrated solution (150 g L^{-1}) was shown to be brightly fluorescent under X-rays (**Figure 2a**), providing a conversion yield of roughly 21 000 photons MeV^{-1} even for 662 keV rays, exhibiting high penetration length. A modified liquid scintillator was proposed in Ref. [18b] by coupling colloidal $CsPbBr_3$ NCs with 2,5-diphenyloxazole, a bright UV dye. Being a strong Lewis base, PPO provides strong binding with lead ions positioned at the NC edges, replacing the native oleic ligands there. The PPO-stabilized HP NCs perform as wavelength shifters (Figure 2b), which provide linear response versus dose rate up to 500 mGy s^{-1} (Figure 2c). Furthermore, the PPO coupling improves stability and allows for obtaining a light yield of 23 300 photons MeV^{-1}. The $CsPbBr_3$ NC solution yields better scintillating properties than $CsPbCl_3$ with lower stopping power and even better than $CsPbI_3$ NCs (Figure 2c) with higher stopping power. Still, it emerges to be clearly overperformed by PPO-HP hybrid composites. Thus, the tactic to improve the efficiency of HP NC-based liquid scintillator by using nonradiative resonant energy transfer between donor and acceptor species, i.e., the Förster effect, seems successful. In Ref. [18c], coupling various organic dyes to $CsPbBr_3$ NCs as high-*Z* X-ray absorbers were tested to obtain hybrid scintillators with enhanced light yield values (Figure 2d). In detail, PPO, 9,10-diphenylanthracene (DPA), p-terphenyl (PTP), and naphthalene (NAP) modified HP NCs were compared. The light yield was increased for all of them, and the maximum value obtained reached 16 700 photons MeV^{-1}. A decay time enhancement (from *c.a.* 25 to 37 ns) was registered but considered not to be crucial.

X-ray detection using scintillating HP NCs usually starts with testing them in colloidal solutions. Zhang et al. prepared $CsPbBr_3$ nanosheets by co-precipitation, which exhibited a strong RL response.[18a] A concentrated solution (150 g L^{-1}) was shown to be brightly fluorescent under X-rays (Figure 2a), giving a conversion yield of ≈21 000 photons MeV^{-1} even for 662 keV rays, exhibiting a high penetration length. A modified liquid scintillator has been proposed in ref. [18b] by coupling colloidal $CsPbBr_3$ NCs with 2,5-diphenyloxazole, a bright UV dye. As a strong Lewis base, PPO provides strong binding with lead ions positioned at the NC edges, replacing the native oleic ligands there. The PPO-stabilized HP NCs act as wavelength shifters (Figure 2b), providing a linear response versus a dose rate of up to 500 mGy s^{-1} (Figure 2c). In addition, the PPO coupling improves the stability and allows a light yield of 23 300 photons MeV^{-1} to be achieved. The $CsPbBr_3$ NC solution gives better scintillating properties than $CsPbCl_3$ with lower stopping power and even better than $CsPbI_3$ NCs with higher stopping power (Figure 2c). However, they are clearly outperformed by PPO-HP hybrid composites. Thus, the tactic of improving the efficiency of HP NC-based liquid scintillators by exploiting the non-radiative resonant energy transfer between donor and acceptor species, i.e., the Förster effect, seems to be successful. In Ref. [18c], the coupling of various organic dyes to $CsPbBr_3$ NCs as high-Z X-ray absorbers was tested to obtain hybrid scintillators with enhanced light yield values (Figure 2d). Specifically, PPO, 9,10-diphenylanthracene,

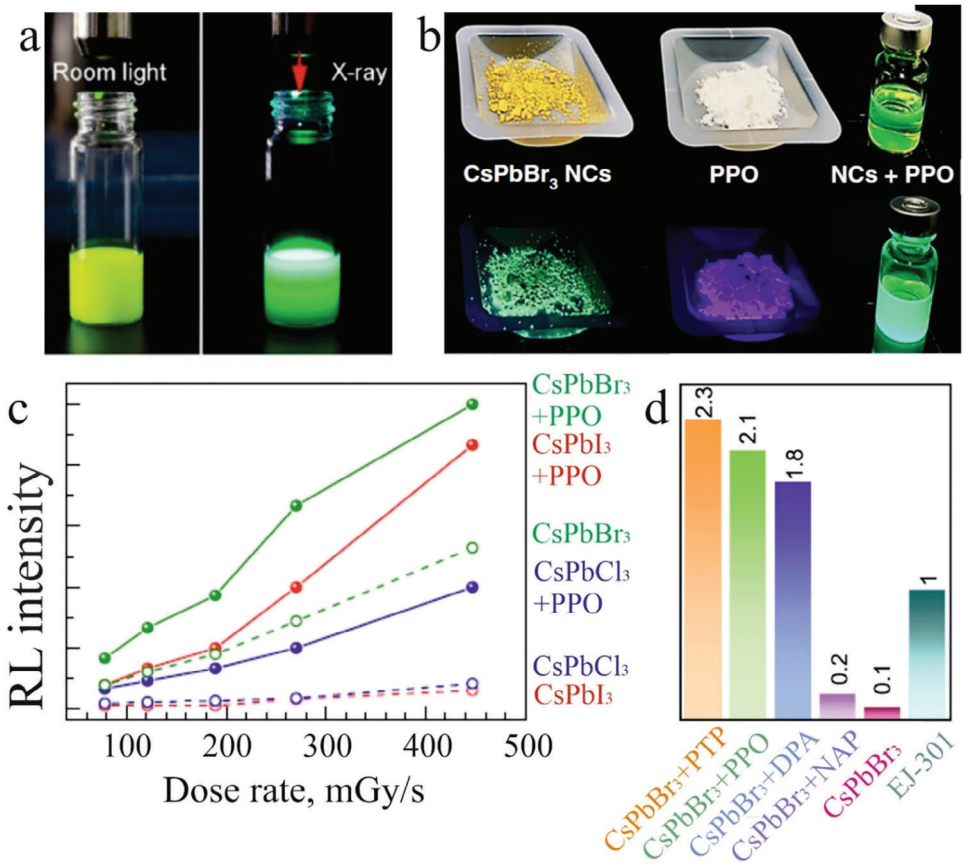

Figure 2. a) Colloidal $CsPbBr_3$ nanosheet solution under daylight and X-rays (Reproduced with permission.[18a] Copyright 2019, American Chemical Society); b) $CsPbBr_3$ NCs, PPO and $CsPbBr_3$ NCs+PPO liquid scintillator under daylight and UV (Reproduced with permission.[18b] Copyright 2020, Springer Nature), c) RL dose dependencies of cesium lead halide NCs in pristine form and dressed by PPO dye (Reproduced with permission.[18b] Copyright 2020, Springer Nature), d) Integrated RL intensities of commercial EJ-301 scintillator, $CsPbBr_3$ NCs in pristine state and covered by PTP/PPO/DPA/NAP dyes (Reproduced with permission.[18c] Copyright 2022, American Chemical Society).

p-terphenyl, and naphthalene modified HP NCs were compared. The light yield was increased for all of them, and the maximum value obtained reached 16 700 photons MeV^{-1}. An increase in lifetime (from ≈25 to 37 ns) was observed but was not considered critical. The hybrids were sensitive to various γ beams (356–1274 keV), providing lower light yields at these high energies. The light yields obtained, ranging from 6 115 for DPA to 8 370 photons MeV^{-1} for PTP dye, is still advantageous for high-energy detection because of the linearity of their detection responses versus the quantum energy of various γ sources.

Liquid scintillators have obvious advantages: low cost, mass scalability, and ease of processing. However, their Förster resonance energy transfer is highly dependent on the stability of the dye-NC and the small coupling distance, which are difficult to maintain in solution, especially at high doses. Additional disadvantages of scintillating solutions that limit the efficiency and spatial resolution of the detector are flocculation in colloids, solvent volatility, Brownian motion, etc. Furthermore, in solution, the scintillating nanocrystals are naturally diluted by the solvents, requiring larger device dimensions to absorb all of the X-ray radiation, which also limits the spatial resolution in imaging devices. Any fractures in the scintillator housings will result in leakage of toxic lead-containing liquid environments, which no user wants. Therefore, the assembly of NCs into a scintillating solid is preferred for any application.

4.3. $CsPbBr_3$ Nanocrystal Assemblies in Scintillating Solids

There are several ways to obtain solid nanocrystal assemblies applicable to scintillator applications. They can be applied as purely nanocrystal solids or they can be incorporated into matrix materials, organic or inorganic, crystalline or amorphous. Of course, the matrix materials have a profound effect on the overall performance of the scintillator by influencing reabsorption, luminescence yield, or environmental stability. Several strategies are discussed in detail below.

4.3.1. Pure $CsPbBr_3$ Nanocrystal Assemblies

While structurally the most perfect form of solids is given by single crystals, self-assembled NC arrangements can even outperform the single crystal HP materials for instance due to the stronger coupling of the wave functions of the individual NCs, eventually providing superradiance.[19] An easy way to integrate

NCs into solids is given by the possibility of preparing thick films simply by drop casting. The sub-nanosecond time of the main decay component (0.67 ns) was achieved by size selection of the NCs used, as the slow decay component is attributed to "thick" nanosheets that adopt the bulk properties of $CsPbBr_3$. More advanced than drop casting is deposition by a doctor blade. A homogeneous $CsPbBr_3$ NC film deposited by doctor blade coating was tested as an X-ray phase contrast imager in Ref. [20a]. The unprotected NCs withstood a dose of 3.6 Gy at a dose rate of 1 mGy s^{-1}, after which they were susceptible to bleaching. The simple oleic acid ligands usually attached during nanocrystal synthesis do not prevent their photodegradation even after exposure to lower X-ray energies of ≈1.5 keV. Therefore, protective ligands or matrices are desirable.[20b] In later work, the long-term stability of NC scintillator films was improved with protective organometallic surfactants[20b] or by changing the shape of the nanocrystals. With their native oleic acid ligands, $CsPbBr_3$ films of nanosheet-shaped NCs were self-assembled by solvent evaporation. These films outperformed conventionally activated sodium halide scintillators in efficiency and provided a fast response with a main decay component of ≈11 ns over a wide range of dose rates up to mGy/s.[20c] The NCs were cast onto flexible substrates of choice, such as polydimethylsiloxane (PDMS), for scintillator preparation, which was placed on a photomultiplier tube (PMT) for detection of the emitted photons (inset in **Figure 3**a). Imaging was demonstrated with a film of 120 µm thickness, and ultralow doses (rates as low as 13 nGy s^{-1}) of X-rays were detected.[20d] The films showed an approximately linear response at high dose rates (10 $nGys^{-1}$–$mGys^{-1}$), and their response saturated at ≈0.1 mm thick films, most likely due to the increasing influence of self-absorption (Figure 3a). This 120 µm NC film outperformed several commercial scintillating materials in luminescence yield, and of CsI:Tl, for example, a 5 mm thick piece was required to compete with the colloidal NCs.

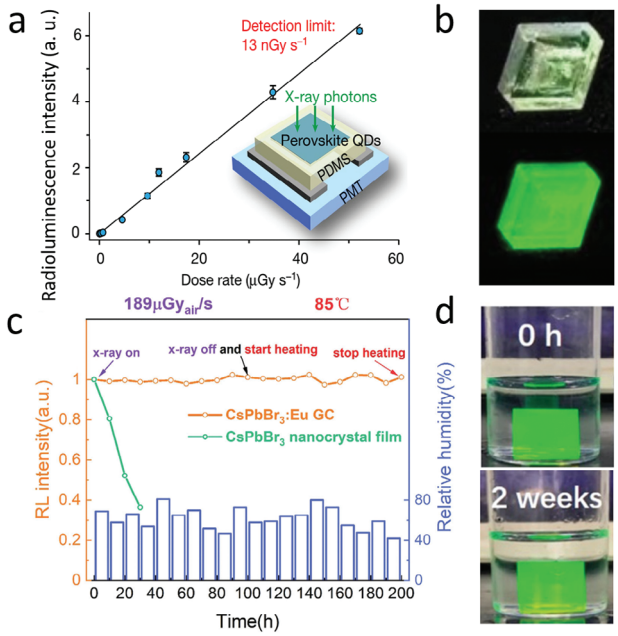

Figure 3. a: RL for a $CsPbBr_3$ NC film-based scintillator as a function of dose rate. The inset shows a sketch of a sandwich detector consisting of $CsPbBr_3$ NC film, a polydimethylsiloxane layer, deposited on a photomultiplier (Reproduced with permission.[20d] Copyright 2018, Springer Nature) b: Photographs of $CsPbBr_3$ NCs embedded in Cs_4PbBr_6 single crystal matrix irradiated by sunlight (top) and 365 nm-LED (bottom). The size of the crystal was ≈8 × 8 × 3 mm (Reproduced with permission.[23a] Copyright 2022, Elsevier B.V.) c: Comparison of RL stability of $CsPbBr_3$ NC film and Europium doped $CsPbBr_3$ NC-in-glass composites under prolonged combined radiation, and thermal stress: arrows indicate X-rays on (first), X-rays-off and start heating (second), terminate heating (third) (Reproduced with permission.[24e] Copyright 2021, Wiley VCH GmbH); d: Water stability of $CsPbBr_3$ in a sodium and zinc modified borosilicate glass (Reproduced with permission.[24g] Copyright 2021, Royal Society of Chemistry).

4.3.2. $CsPbBr_3$ Nanocrystals in Organic Polymer Matrix

As a further development of nanocrystal films, the $CsPbBr_3$ NCs were embedded in polymers. For example, the nanocrystals were embedded in a poly(methyl methacrylate) PMMA film that was mechanically attached to an organic photodetector. This combination was investigated as a proof-of-concept for a flexible indirect X-ray detector.[20e] The active layer of the organic photodiode was chosen to be ≈2 µm thick. With the attached NC in PMMA film, the detector is sensitive to 100 µGy x-ray doses. While this value is by no means a record, the PMMA-$CsPbBr_3$-NCs composite approach proved very attractive in a device geometry reminiscent of commercial devices in which the scintillator is packed directly onto a photodetector array and protected by a carbon fiber-reinforced polymer film. For these devices, the X-ray absorption efficiency has been optimized up to 80%. Such a device showed a luminescence efficiency of up to 177 000 photons MeV^{-1}, the highest value ever reported for perovskite materials, and a linear conversion dependence for dose rates up to 0.6 mGy s^{-1}.[20f] The $CsPbBr_3$ NC scintillator lost only 4% of its initial conversion value after the stability test at a radiation dose of 40 Gy s^{-1}, which is comparable to the sensitivity loss observed for commercial gadolinium oxysulfide scintillators. Imaging with this scintillator has also been demonstrated and better lateral resolution has been reported compared to a commercial gadolinium oxysulfide scintillator or even an amorphous selenium direct conversion imager. As an alternative, embedding in polystyrene was demonstrated in Ref. [21c]. Special care was taken to avoid any aggregation of the $CsPbBr_3$ NCs within the matrix, which was achieved by using different ligands. The ligand exchange to didodecyldimethylammonium bromide allowed a 10% filling factor in the polymer with reduced scattering compared to the original oleic acid and oleylamine-capped NCs.[21c] Instead of a pure polystyrene matrix one with small amounts of additional organic species (2-(4-tert-butylphenyl)−5-(4-phenylphenyl)−1,3,4-oxadiazole) was used, and instead of pure $CsPbBr_3$ NCs also $CsPb(Cl/Br)_3$ NCs emitting at shorter wavelengths were incorporated which allowed to enhance the faster and suppress the slower luminescence decay channels in the scintillator.[21d]

Embedding into an organic matrix is a strategy that is also highly suitable for combining the $CsPbBr_3$ nanocrystals with organic downshifters, as described above for $CsPbBr_3$ nanocrystals in solution. In a recent example, $CsPbBr_3$ nanocrystal sheets were shown to be potent X-ray sensitizers for directly attached organic chromophores exhibiting thermally activated delayed fluorescence (TADF chromophore).[22a] The luminescence in the

chromophore is excited by interfacial energy transfer. TADF chromophores are one of the best candidates for luminescent centers due to their minimized singlet-triplet energy gap.[22a] This allows them to utilize both singlet and triplet excitons for light emission through highly efficient spin upconversion from nonradiative triplet states to radiative singlet states. Difluoroboron 1,3-diphenylamine β-diketonate was chosen as the chromophore, which contains 2 fluorine atoms that can form strong bonds with the lead atoms (F-Pb) within the $CsPbBr_3$ nanosheet, ensuring efficient interspecies energy transfer to enhance emission. The donor-acceptor structures were incorporated into PMMA films, which acted as scintillating films with a low detection limit of ≈39 nGy s^{-1}.[22a] An important feature of this donor-acceptor approach in a polymer matrix is that the emission is virtually nonabsorbing and thus loss-free. This has been demonstrated in detail in Ref. [22b] by combining the $CsPbBr_3$ nanocrystals as sensitizers with a perylene dye called 9,9-bis[perylene-3,4-dicarboxylic-3,4-(N-(2,5-di-tert-butylphenyl)], which was chosen as emitter due to its perfectly aligned highest occupied molecular orbital and lowest unoccupied molecular orbital with the valence and conduction bands of $CsPbBr_3$. The scintillator was tested to provide a decent photon yield of ≈10 000 photons MeV^{-1} and a short emission lifetime of 3.4 ns. In a PMMA-based waveguide, the propagation of radioluminescence from a scintillator film was shown to exhibit low losses on a > 10 cm scale, demonstrating the reabsorption-less property of the composite scintillator. Similar composite scintillators based on $CsPbBr_3$ nanocrystals and an organic wavelength shifter have been tested for X-ray imaging and in so-called radioluminescent nuclear batteries. The latter contains a radionuclide as an energy source, whose radiation is converted by a scintillator into the UV/Vis spectral range. The generated light is then harvested by a highly efficient solar cell, possibly based on epitaxial III/V semiconductor single or even multijunction devices. In Ref. [22c] such a battery has been simulated and tested using $CsPbBr_3$ NCs in PMMA matrix combined with an organic dye, PPO, as a wavelength shifter to match the spectral response of the chosen solar cell. As a result, it was demonstrated that $CsPbBr_3$ nanocrystals can be used as a wavelength shifter to control the emission spectrum of PPO and significantly improve the overall performance of the radioluminescent nuclear battery.

4.3.3. $CsPbBr_3$ Nanocrystals in Inorganic Crystalline Matrix

Since the embedding of colloidal perovskite NCs in organic matrix materials resulted in scintillators with promising properties in terms of photon yield, radiation hardness, and dynamic behavior, the question arises of how such a strategy could be further improved. One possibility would be to embed the ABX_3 NCs in inorganic matrix materials, at best in the form of single crystals. In this case, the matrix material has to be chosen in such a way that a close lattice match with the NCs is achieved in order to obtain perfect interfaces and thus NC surface passivation. A promising attempt in this direction was reported in,[23a] where single crystals were grown by a solvent-cooling method. By using a special temperature cooling profile with a hold at ≈70 °C to nucleate the growth of nanocrystals at this stage, mm-sized Cs_4PbBr_6 single crystals with embedded $CsPbBr_3$ NCs were obtained (Figure 3b), exhibiting luminescence with a quantum yield close to 80%. This resulted in excellent scintillator parameters with a photon yield of 15 290 photons MeV^{-1}, a linear response as a function of irradiance, and a low detection limit. In addition, the average emission lifetime was short (12.8 ns), indicating a low concentration of radiation-induced trap states. Ref [23b] reports light yield parameters for $CsPbBr_3$ embedded in Cs_4PbBr_6 in the form of nanocrystals instead of single crystals. Their performance was tested under γ radiation exposure, providing 64 000 photons MeV^{-1} and an average emission lifetime of less than 10 ns. In addition, energy-resolved detection was demonstrated with a resolution significantly better than commercial NaI(Tl) scintillators, highlighting the advantages of $CsPbBr_3$ nanocrystals when properly passivated by a shell or inorganic matrix. The overall advantages of such a $CsPbBr_3$ in inorganic wide bandgap matrix strategy have been discussed in Ref. [23c] as i) higher X-ray stopping power of the host matrix compared to low-Z glasses and acrylates used as matrixes; ii) protection of the nanocrystalline emitters from degradation; iii) suppression of reabsorption via higher Stokes shift; iv) activation of the wide bandgap host to low bandgap guest excitation transfer; and v) facilitation of device processing and complexity reduction, since both host and guest are derived from the same raw precursors. Thus, as with the organic matrix, an inorganic matrix for $CsPbBr_3$ offers several promising advantages and thus represents a research avenue worth pursuing. In addition to high photon yield and low detection limit, stability has also been achieved, which is an important component for X-ray detectors in modern applications. What remains to be improved is the spatial resolution of scintillating detectors. In CsI:Tl scintillators, arrays of oriented columnar structure are often grown, with each column acting as both an X-ray converter and an optical waveguide. Similar structures have been obtained from perovskites.[23d–e] In particular, single crystalline nanowires were fabricated by infiltrating a perovskite precursor solution into the pores of commercially available anodized aluminum oxide (AAO) membranes.[23d] This templated grown nanowire array with more or less regular spacing between the wires allowed X-ray imaging with a spatial resolution of ≈160 lp mm^{-1} at modulation transfer function (MTF) = 0.1, which is nominally better compared to CsI(Tl). Besides 2D imaging, even 3D X-ray tomography with µm resolution has been demonstrated; however, the required illumination times were too long for practical applications due to a too-short wire length and thus a too-low light yield.[23e]

4.3.4. $CsPbBr_3$ Nanocrystals in Inorganic Glass Matrix

Several references use a melt-quenching approach to achieve nucleation and growth of perovskite NCs within various types of glasses.[24a–c] The first to use such perovskite in a glass matrix were probably Wang et al.,[24c] who not only showed scintillation with different colors depending on the halide composition, but also a long lifetime. They also showed that radiation-induced damage to the scintillator can be healed by reheating it to the glass transition temperature, making these devices reusable. Improvements of the $CsPbBr_3$ in the borosilicate glass experiment were achieved in terms of homogeneous distribution of the nanocrystals within the matrix, resulting in reduced scattering, and in PL quantum yield by light doping with europium. In such a hybrid

assembly, europium is partially incorporated into the lattice of HP NCs, resulting in a slight shrinkage of its lattice. A similar glass has been thoroughly tested for stability and degradation in Ref. [24e], where X-ray imaging with a remarkably high resolution of 15 lp mm^{-1} was demonstrated. The $CsPbBr_3$:Eu^{3+} NCs glass composites have a reasonable stopping power for X-rays up to 300 keV, a negligible afterglow, stable characteristics almost independent of the ambient humidity, and elevated temperature conditions (Figure 3c) withstanding up to tens of mGy accumulated doses. The stabilizing dopant does not necessarily have to be europium, as shown in Ref. [24f], where $CsPbBr_3$ NCs were doped with lutetium ions. In such NCs-in-borosilicate glass composites, the NCs are uniformly distributed, resulting in highly transparent and waveguiding samples. The incorporation of Lu^{3+} into the NCs stimulates a fast response with decay times of 27 ns and low detection limits of 50 nGy s^{-1}. As already discussed for undoped $CsPbBr_3$ NCs in a glass matrix,[24c] the authors here introduce thermal healing processes that allow the healing of various photodamages in the detectors caused by high-dose X-rays, ultraviolet, and daylight irradiation. The $CsPbBr_3$ NCs described in Ref. [24g] were crystallized inside sodium and zinc-modified borosilicate glass and not only showed that they operate with increased environmental stability and water resistance over weeks (Figure 3d) compared to colloidal nanocrystal films but also highlighted the possibility to fabricate fibers from such glass-ceramics. As an important argument for possible commercialization, the cost of the $CsPbBr_3$-in-glass approach was also estimated to be significantly lower than that of $Bi_4Ge_3O_{12}$ single crystals. A special case is $CsPbBr_3$ NCs precipitated in tellurite glasses due to their relatively high refractive index, which is close to that of the embedded NCs. This should reduce scattering and improve transparency. Unfortunately, the PLQY in such a ceramic-glass composite was limited to ≈7%, partly caused by self-absorption due to the small PL Stokes shift of the embedded NCs. The advantages of the $CsPbBr_3$ in telluride glass are an almost linear dependence of RL versus X-ray flux and only low X-ray darkening and thermal quenching of RL.[24h] Furthermore, the lower melting and glass transition temperatures of the telluride glass as compared to the borosilicates make its preparation less energy-consuming.

From section 4.3 it can be concluded that $CsPbBr_3$ is excellently suited for scintillator applications, regardless of whether the nanocrystals are present as a pure nanocrystal assembly or whether they have been embedded in various matrix materials. $CsPbBr_3$ is sufficiently stable and has a sufficiently high melting point so that all these treatments can be carried out. $CsPbBr_3$ always shows excellent emission behavior and is therefore probably the most important material for scintillators made of perovskite semiconductors. However, there are also alternatives, especially inorganic-organic hybrid perovskites, whose suitability as X-ray scintillators has of course also been investigated.

4.4. Alternative Lead-Halide Perovskites to $CsPbBr_3$

As mentioned above, the 3-D lead halide perovskite $CsPbBr_3$ is primarily used in NCs, especially in scintillator applications, and any deviation from this composition generally results in NCs with less convincing properties. Changing the halide from bromine to chlorine already leads to strongly changed properties, not only regarding the emission wavelength. This was demonstrated with $CsPb(Cl,Br)_3$ NCs embedded in borate glass, which exhibited much higher PLQY for either pure bromine or bromine-rich HPs than for chlorine-rich ones. The latter exhibits much faster emission, which is attributed to the predominance of non-radiative recombination.[25a] While NCs prepared by precipitation within a glass matrix at high temperatures are expected to exhibit predominantly non-radiative recombination due to the lack of sufficient surface passivation, a large difference between the PLQY of bromides and chlorides was also observed in colloidal NC solutions of $FAPbBr_{3x}Cl_{3(1-x)}$ synthesized by ligand-assisted precipitation (**Figure 4a**).[25d] To obtain transparent plastic scintillators (Figure 4b) with low scattering, the NC was covered with bis(2-(methacryloyloxy)ethyl) phosphate (BMEP) ligands, which allowed the nanocrystals to couple to the polymer matrix during polymerization. $FAPbBr_3$ NCs were embedded in an EJ-290 plastic scintillator and compared with a $FAPbBr_3$/PMMA nanocomposite, which showed superior performance in terms of both photon yield and luminescence decay time, which was found to be in the order of ≈150 ns. X-ray imaging was also successfully demonstrated with the $FAPbBr_3$/PMMA nanocomposite (Figure 4c). However, to compete with $CsPbBr_3$, the novel $FAPbBr_3$/PMMA nanocomposite must be significantly brighter to overcome the reduced X-ray stopping power, which may be difficult to achieve. For this reason, hybrid HP nanocrystals with and without Cs have been developed for scintillating detectors of radiation other than X-rays. While the nanocrystals described in Refs. [25a,d] were tested with an 80 kV X-ray source, and the following NC scintillators have been demonstrated for fast neutron imaging,[25b] and for gamma radiation detection,[25c,e] respectively. Both scintillators are NCs in solution. The attractive feature of the Mn^{2+}–doped $CsPb(BrCl)_3$ NCs in Ref. [25b] is the Stokes-shifted radiation, which is observed with quantum yields up to ≈60% for a Br content x≈0.5 (Figure 4d), allowing for nearly self-absorption-free emission. This feature, together with the possibility to obtain relatively highly concentrated solutions, shows the potential of Mn^{2+}:$CsPb(BrCl)_3$ NCs to replace the currently used ZnS:Cu NCs as the leading scintillator for fast neutron imaging. Ref. [25c] discusses the use of perovskite NCs for neutrino detection but uses a gamma-ray source to demonstrate the feasibility of HP NCs as wavelength shifters in a liquid scintillator. The primary scintillator is 2,5-diphenyloxazole in a toluene solution at a concentration of 1 g L^{-1}. The nanocrystals used are platelets with a composition of $L_2[MAPbBr_3]PbBr_4$, where L is a ligand such as n-butylammonium or n-octylammonium. The addition of these NCs to the PPO scintillator allows to obtain a two-color emission, which is dominated by the perovskite emission only at high concentrations. For applications such as neutrino detectors, the described liquid scintillators still require many improvements.

The observation that perovskite NC materials are suitable for scintillator applications for different high-energy radiations with the same device was demonstrated by Datta, Fiala, and Motakef,[25e] who used a 2-D perovskite based on lithium-alloyed phenethylammonium lead bromide (PEALPB). The advantage of lithium is that it absorbs thermal neutrons, passivates trap states, and thus increases the light yield. In addition to scintillation by

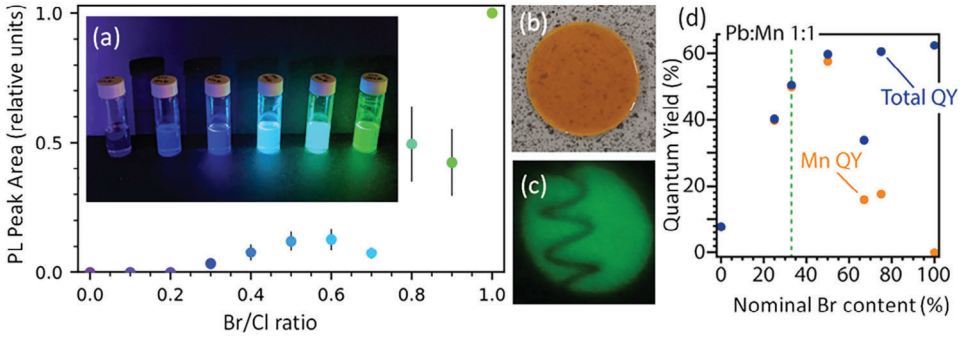

Figure 4. Lead-perovskite nanocrystals. a) The integrated photoluminescence intensity measured for $FAPbBr_{3x}Cl_{3(1-x)}$ NCs as function of the Br/Cl x. Inset: Photograph of dispersed $FAPbBr_{3x}Cl_{3(1-x)}$ NCs under UV light; from left to right: x = 0, 0.2, 0.4, 0.6, 0.8, 1. b) Photograph of $FaPbBr_3$ NCs embedded in a plastic scintillator. c) X-ray image of a metal spring, acquired using the 1.8 wt.% loading $FAPbBr_3$/PMMA nanocomposite scintillator (Reproduced under terms of the CC-BY license.[25d] Copyright 2022, The Authors, published by MDPI). (d) Photoluminescence quantum yield of a 50% Mn-doped sample series of $CsPb(BrCl)_3$ NCs as a function of Br content (blue dots – total quantum yield, orange dots–quantum yield of Mn^{2+} emission (Reproduced with permission.[25b] Copyright 2021, American Chemical Society).

X-ray excitation, the PEALPB was also shown to detect gamma rays and neutrons. The special highlight of Ref. [25e] is that the perovskite was filled into a microcapillary plate to obtain an array of 1.2 mm long hexagonal rods with lateral dimensions down to 20 microns (**Figure 5a**). These arrays mimic the columnar growth of commercial CsI:Tl detectors and allow the improvement of lateral resolution for X-ray imaging due to waveguiding effects in each of these microcapillaries. By combining this structured scintillator plate with a Si-based pixelated photodiode array X-ray images could be taken. As a result, high-resolution X-ray imaging was achieved, as illustrated by an image of a USB flash drive (Figure 5b). A modulation transfer function was measured as a function of spatial frequency and compared favorably with those obtained by other direct and indirect X-ray imagers (Figure 5c). This ultra-high resolution, which is promising for a wide range of applications, was achieved in Ref. [25e] using single crystals grown in the microcapillaries, and thus it is an open question whether similar or even better results could be obtained using NCs made of the same material or other perovskites.

4.5. Radiation Hardness and Self-Healing of Lead-Halide Perovskite Nanocrystals

What remains to be improved for metal halide perovskite nanocrystal scintillators is stability. A milestone in this direction was reported by Brovelli's group,[21a] which demonstrated a combination of extreme γ-ray hardness and high scintillation yield. This achievement was made possible by post-synthetic fluorination of the nanocrystal surface to reduce surface trap states, resulting in a fivefold increase in scintillation efficiency. The scintillation efficiency of the $CsPbBr_3$ NCs changed only insignificantly with the absorbed dose of up to 1 MGy delivered by a non-monochromated ^{60}Co source,[21a] a dose equivalent to the annual dose accumulated by the inner walls of a nuclear reactor chamber and by the inner magnetic coil of the Large Hadron Collider at CERN. The relevance of these results to X-rays used for medical imaging is still questionable. However, the low radiation damage observed for the non-monochromated ^{60}Co source is still surprising, considering that the plastic vials in which the nanocrystals were kept during the irradiation experiment eventually appeared brittle, whereas the $CsPbBr_3$ remained almost unaffected. The low radiation damage could also be attributed to another amazing ability of HPs, which has been described as a self-healing phenomenon. The effect has been clearly demonstrated in bulk single crystals for various $APbBr_3$ perovskites.[21b] Here, the damage was induced deep in the material by 2-photon absorption, resulting in bleach in the luminescence of the samples, which recovered on different time scales depending on the chosen perovskite materials. These self-healing phenomena may be related to the diffusion of ions within the single crystals, healing previously generated point defects. An important point for self-healing is that after damage, no species provided by the damage can escape from the spatial region of damage. This condition is provided in the single crystals, and damage is induced deep in the volume by the surrounding crystalline material. Self-healing was also briefly discussed for lead-halide perovskite nanocrystals. Even though this is possibly not a very clear demonstration of self-healing, the high photoluminescence quantum yield and the long stability of $CsPbBr_3$ nanocrystals in polar solution have been ascribed to a ripening effect, which can heal surface defects.[25f] Clearer evidence for self-healing in lead-halide nanocrystals was given for $MAPbBr_3$ encapsulated in NiO nanotubes. In the study by Kamau et al.[25g] A decrease in the perovskite's luminescence intensity was observed as a function of illumination duration by a UV laser. The reduced luminescence intensity, however, recovered after the laser was switched off for several hours. Self-healing of lead-halide perovskite nanocrystals has been reported also several times for cases where the nanocrystals have been incorporated into the polymer matrix. In this case, however, more of the self-healing properties of the polymers have been demonstrated than those of the nanocrystals, for instance, the healing of a scratch in the composite, as was demonstrated in Ref. [25h]. It should be noted, however, that there are very clear demonstrations of self-healing in lead-free perovskite nanocrystals and related lead-free materials, as will be discussed in chapter 5.1.

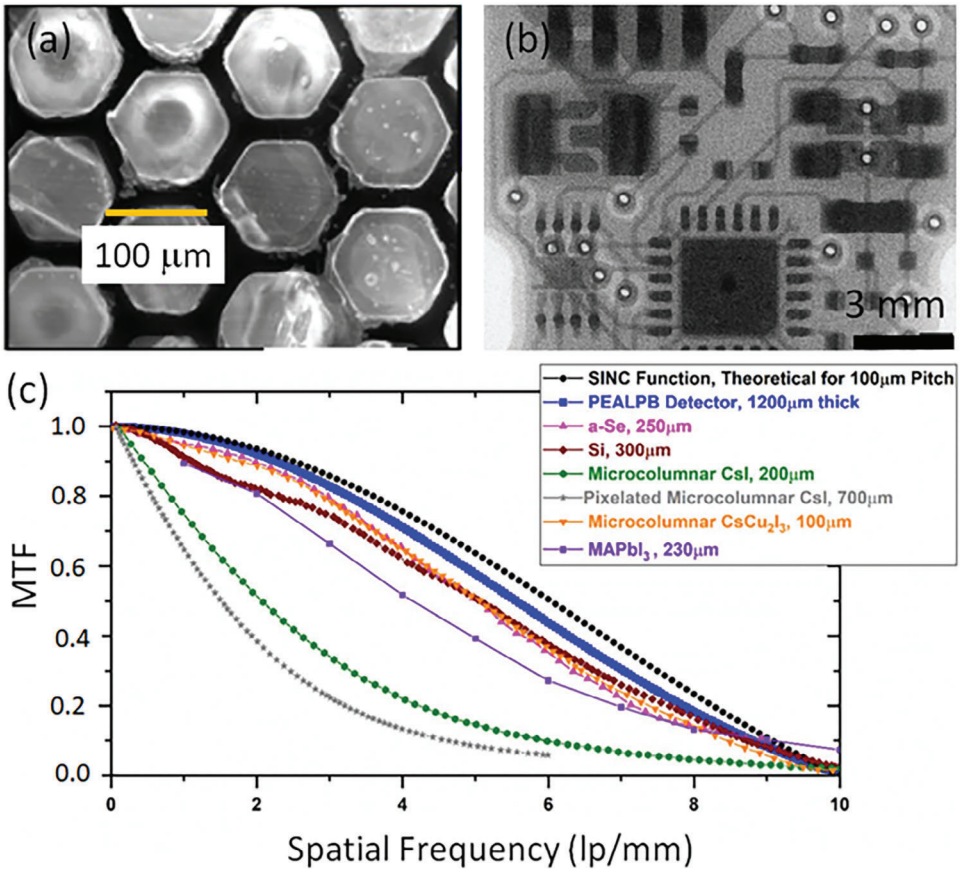

Figure 5. Imaging detector based on a 2-D perovskite, based on lithium-alloyed phenethylammonium lead bromide (PEALPB). a) Plan view of a single-crystalline PEALPB scintillator array produced by filling a borosilicate glass microcapillary plate. b) Electronic circuits within a USB drive visualized by X-ray imaging with a PEALPB array of hexagonal microrods. c) Modulation transfer function of PEALPB array-based X-ray detector along with MTF functions of other state-of-the-art detectors with relatively lower thicknesses. The sync function plot corresponds to the theoretical MTF function of a 100 µm pixel pitch, shown as a reference (Reproduced with permission.[25e] Copyright 2021, Springer Nature).

5. Scintillating Detectors Assembled from Lead-Free HP NCs

The primary strategy for improving HP NCs is to eliminate reabsorption – an obstacle that becomes relevant when thick films are assembled, as required for X-ray absorption, or when highly concentrated solutions of NCs are used as scintillators. Remarkable progress has been made with $Cs_3Cu_2I_5$ NCs, a 0D quasi-HP family member. To date, reliable low-temperature syntheses have been demonstrated to achieve reasonable size and shape control of the NCs. Most importantly, the high Z values of $Cs_3Cu_2I_5$ were combined with shorter luminescence decay times and higher luminescence quantum yields than for $Cs_3Cu_2Br_5$ and $Cs_3Cu_2Cl_5$ NCs.[26a] With Stokes shift values above 1 eV, these NCs are best suited as lead-free substituents for $CsPbBr_3$ among many HP NCs.[26b] $Cs_3Cu_2I_5$ NC scintillators are linearly sensitive to X-ray exposures as colloidal solutions and drop-cast films (**Figure 6a**) for dose rates between 13.4–94.1 µGys^{-1} and yield a remarkable 79 000 photons MeV^{-1} to overcome many industrial SC scintillators.[26a] Due to the confined exciton within the 0D $[Cu_2I_5]_3$ clusters, where the cluster orbitals do not overlap, the spectral regions of emission and excitation of $Cs_3Cu_2I_5$ NCs are narrow and significantly separated. Thus, reabsorption is not observed even in rather dense NC assemblies. The nanocrystals have been tested for environmental stability over several months and under operational conditions for several days. Thus, $Cs_3Cu_2I_5$-based scintillators could be used for X-ray imaging and computed tomography with impressive results. Figure 6c,d shows a reconstructed 3D image next to one of the measured projections, revealing the shape of a snail with fine details. Although the stability of $Cs_3Cu_2I_5$ NCs was found to be sufficient for computed tomography experiments,[26b] it was further improved in Ref. [26c] (Figure 6e) together with the PLQY (up to 87%) by dispersing $Cs_3Cu_2I_5$ NCs in transparent styrene matrices. The controlled polymerization allowed the fabrication of a wide-area scintillator to detect dose rates as low as 63 nG y$^{s\text{-}1}$.[26c] As in the case of lead HP nanocrystals, stability improvements can also be achieved for lead-free HP NCs by embedding them in a glass matrix. Thus, a series of lead-free cesium-manganese HP NCs ($CsMnCl_3$, $CsMnBr_3$, and Cs_3MnI_5) have been prepared in Ref. [26d] in a boron-aluminum-calcium glass matrix by simple melt quenching methods. The $CsMnCl_3$ NCs exhibited the highest radioluminescence intensity and PLQY of 41.8%. The NCs-in-glass composites exhibited a linear response to X-ray excitation dose rates from 0.5 to 162 mGy s^{-1} (Figure 6b) with a detection limit of 470 Gy s^{-1}.[26d] In addition, high-resolution

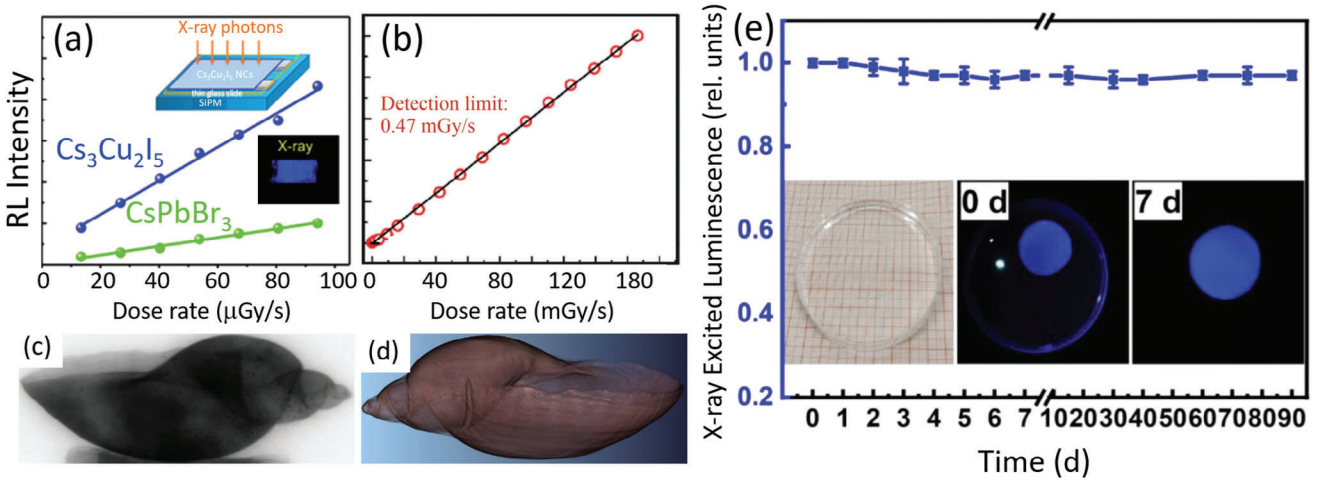

Figure 6. Performance of lead-free perovskite nanocrystals in scintillating detectors. a) RL intensity of $Cs_3Cu_2I_5$ NCs and $CsPbBr_3$ NCs as a function of X-ray dose rate; a photograph of $Cs_3Cu_2I_5$ NC film under X-ray excitation is shown as insert (Reproduced with permission.[26a] Copyright 2020, Wiley VCH GmbH); b) RL intensity response of $CsMnCl_3$ NCs-in-glass composite (Reproduced with permission.[26d] Copyright 2022, Wiley VCH GmbH). c,d) X-ray image and reconstructed 3D computed tomography image of a snail, obtained with a scintillator based on $Cs_3Cu_2I_5$ nanocrystals (Reproduced with permission.[26b] Copyright 2021, Wiley VCH GmbH). e) Relative light output of a $Cs_3Cu_2I_5$—in polystyrene matrix immersed in water. The inset is a photographic image during continuous immersion of such a screen in water for 0 and 7 days under 265 nm UV light (Reproduced with permission.[26d] Copyright 2022, Wiley VCH GmbH).

imaging was demonstrated along with excellent long-term stability. A key to the high-performance scintillators was a large Stokes shift between absorption due to interatomic Mn transitions and emission from STEs.

As mentioned, STEs are also a tool to achieve luminescence with high quantum yield in lead-free double perovskites. Luo et al.[26e] demonstrated warm white light-emitting powders of $Cs_2(Ag_{0.60}Na_{0.40})InCl_6$ with 0.04 percent bismuth doping, which is stable for 1000 h of operation and provides PLQY of 86%. This system, namely $Cs_2Ag_xNa_{1-x}Bi_yIn_{1-y}Cl_6$, now abbreviated as CANBIC, was recently developed further by Stroyuk et al.[26f] This perovskite synthesized with x = 0.3–0.4 and y = 0.01–0.02 showed a champion room-temperature PLQY of 98% ± 2% as well as a prominent environmental stability. Further, films were prepared from these powders by thermal evaporation from a single source.[26g] The CANBIC films produced from the most luminescent CANBIC powders exhibited a PLQY of 85%, which is, to the best of our knowledge, the highest value reported for a transparent nanocrystalline film of a lead-free double perovskite so far. The feasibility of transferring CANBIC double perovskites from strongly scattering microcrystalline powders to transparent and uniform nanocrystalline films while preserving the composition will be highly beneficial for applications – possibly including X-ray imaging vial scintillation.

As mentioned above, STEs are also a tool to achieve high quantum yield luminescence in lead-free double perovskites. Luo et al.[26e] demonstrated warm-white light-emitting powders of $Cs_2(Ag_{0.60}Na_{0.40})InCl_6$ with 0.04% bismuth doping, which is stable for 1000 h of operation and provides PLQY of 86%. This system, namely $Cs_2Ag_xNa_{1-x}BiyIn_{1-y}Cl_6$, now abbreviated as CANBIC, was recently further developed by Stroyuk et al.[26f] This perovskite, synthesized with x = 0.3–0.4 and y = 0.01–0.02, exhibited a champion room temperature PLQY of 98% ± 2% as well as outstanding environmental stability. In addition, films were prepared from these powders by single-source thermal evaporation.[26g] The CANBIC films prepared from the most luminescent CANBIC powders exhibited a PLQY of 85%, which, to the best of our knowledge, is the highest value reported to date for a transparent nanocrystalline film of a lead-free double perovskite. The ability to transfer CANBIC double perovskites from highly scattering microcrystalline powders to transparent and uniform nanocrystalline films, while maintaining the composition, will be highly beneficial for applications – possibly including X-ray imaging vial scintillation.

So far, however, X-ray imaging has been demonstrated with CANBIC wafers of various thicknesses between 0.1 and 0.6 mm, formed by pressing powders.[26h] By controlling the content of the heavy atom Bi^{3+}, the X-ray absorption coefficient, radiative emission efficiency, light yield, and light decay were manipulated to maximize the scintillator performance. A light yield of up to 39000 ± 7000 photons MeV^{-1} was obtained for X-rays generated by 50 kV accelerating voltage. These wafer scintillators demonstrated static and dynamic imaging with a low detection limit of 19 nGy_{air} s^{-1} and essentially no afterglow, qualifying this scintillator as a potential candidate for low-dose, real-time X-ray imaging. While NCs of CANBIC have not yet been applied to X-ray scintillation, there are several other lead-free double perovskite nanocrystals with promising X-ray responses. One strategy that has been successfully applied to improve these double perovskite NCs is to dope them. For example, the $Cs_2NaBiCl_6$ NCs presented in Ref. [26i] were doped with Mn. While the UV absorption in these nanocrystals is due to $6s^2 \rightarrow 6s^16p^1$ transitions in the $[BiCl_6]^{3-}$ octahedra, the emission is found at 586 nm due to interatomic transitions in the Mn. Energy transfer from dark STE states enables this luminescence with a decay time of 1.2 ms. The $Cs_2NaBiCl_6$:Mn NCs were incorporated into PMMA films and tested as X-ray scintillators, exhibiting a linear response scaling with dose rates with a detection limit dependent on the

Table 1. Comparison of main parameters of X-(γ-) ray detection assemblies based on halide perovskite nanocrystals.

Detector Structure	X-ray Energy, keV	Range of Linear Response, $\mu Gy_{air}\ s^{-1}$	Detection Limit, $nGy_{air}\ s^{-1}$	Light Yield, photons MeV^{-1}	Refs.
$CsPbBr_3$ LS and drop casted films	<662	1–140		21 000	[18a]
$CsPbBr_3$ PPO LS	10–6000	10 000–500 000		23 300	[18b]
$CsPbBr_3$ PTP LS	<1274			16 740 (X) 8370 (γ)	[18c]
$CsPbBr_3$ film dr Blade	20–60	0.15–50 000	50		[20a]
$CsPbBr_3$ spin-casted	25–85	10–200			[20b]
$CsPbBr_3$ spin casted	10–662	0.02–60	13		[20d]
$CsPbBr_3$ in PMMA	20–80	1000–100 000	160		[20e]
$CsPbBr_3$ in PMMA	10–50	25–350		177 000	[20f]
bi-ligand $CsPbBr_3$ in PMMA	20–1250			8500	[21a]
$CsPbBr_3$ NCs coupled with A^4 chromophore	50	4–208	39		[22a]
$CsPbBr_3$ NCs in Cs_4PbBr_6 SC	30–50	1–30	130	15 290	[23a]
$CsPbBr_3$ NCs in Cs_4PbBr_6 SC	40–59.6			64 000	[23b]
$CsPbBr_3$ NCs in AAO templates	40–45			5300	[23d]
$CsPbBr_3$ NCs in Eu-activated boron silicate glass	50	35–105			[24d]
$CsPbBr_3$ NCs in Eu-activated boron silicate glass	50	25–200		40 100	[24e]
$CsPbBr_3$ NCs in Lu-activated boron silicate glass	40	10–8000	50		[24f]
$Cs_3Cu_2I_5$ NCs drop casted films	50	13–95		79 200	[26a]
$Cs_3Cu_2I_5$ NCs in styrene matrixes	50	10–250	63		[26c]
$CsMnCl_3$ NCs in aluminoborate glass	50	500–17 000		13 400	[26d]
$Cs_2NaBiCl_6$:Mn NCs in PMMA matrixes	50	7.5–98	45.2	28 350	[26i]
Cs_3TbCl_6:Sb NC wafers	22	6–18	212	20 300	[26j]
$Cs_2NaTbCl_6$:Sb NC wafers	22	1.5–18	140	23 500	[26k]
Cs_2HfCl_6 MCs film by a doctor blade then pressed up	50	0.02-7000	55	21 700	[28f]
Cs_2HfCl_6:Te^{4+} MCs in epoxy matrixes	40	3-20	36	76 200	[28a]
Cs_2ZrCl_6:Lu^{3+} MCs in epoxy matrixes	20–60	0.05–8000	15.8	94 190	[28b]
Mn^{2+} activated $Cs_2CdBr_2Cl_2$ MCs in PDMS matrixes	45	10–220	17.8	64 950	[28e]
$Cs_5Cu_3Cl_6I_2$ MCs in PDMS matrixes	40	0.02–8000	60,9	59 700	[28j]
$(C_8H_{17}NH_3)_2SnBr_4$ MCs in PMMA matrixes	40	100–6000			[29a]
$(C_8H_{17}NH_3)_2Cu_2Br_4$ MCs pressed up into ceramic wafer	50	0.01–100	51.1	91 300	[29b]
$Cs_2Ag_xNa_{1-x}InCl_6$:Bi SC wafers	22	1–189	19	39 000	[26h]
Cs_2NaYCl_6:Sb SCs	50	2.5–25	143	22 500	[26l]
Rb_2CuBr_3 SCs	15–50	0.025–16	121	91 056	[28c]
K_2CuBr_3 SCs	50	0.05–15	132.8	23 806	[28g]

thickness of the PMMA film down to 45 $nGy_{air}\ s^{-1}$. The light yield was found to be 28 350 photons MeV^{-1} comparable to many other HP NC scintillators (see **Table 1**).

Contrary to the case of $Cs_2NaBiCl_6$, where an STE enhances the emission of the Mn dopant by energy transfer, in Cs_3TbCl_6 doped with antimony, the dopant allows the formation of an STE that enhances the intrinsic emission of the nanocrystals, in this case, due to interatomic transitions of the intrinsically incorporated lanthanide.[26j] Basically, the same is also observed in $Cs_2NaTbCl_6$: Sb^{3+} NCs.[26k] Interestingly, it is certain that antimony doping, or rather alloying (with concentrations up to 10%), increased the PLQY of Cs_3TbCl_6 NCs to almost 50%.[26j] Both Cs_3TbCl6:Sb^{3+} and $Cs_2NaTbCl_6$:Sb^{3+} exhibit high environmental stability and were therefore tested for scintillation with similar light yields and detection limits (see Table 1). This may be due to the fact that the introduction of the alkali cation (A^+ coordination) allows for a change in the band gap, while an interplay of trivalent cations at the B^{3+} position determines the emission properties. The Sb doping has a similar positive effect on the Cs_2NaYCl_6:Sb^{3+} as on the $Cs_2NaTbCl_6$:Sb^{3+}. While no luminescence could be observed in NCs of the undoped material, the Sb-doped crystals show a sky-blue emission with an optimum PLQY above 50%.[26l] The NCs emission was even surpassed by that of single crystals of the same composition, allowing PLQYs > 82%. Thus, the scintillation properties of the SC materials were tested and are shown in Table 1.

Nevertheless, yttrium-based and possibly also gadolinium-based[26m] double perovskites are valuable targets for future NC investigations in the field of scintillation, perhaps with enhanced

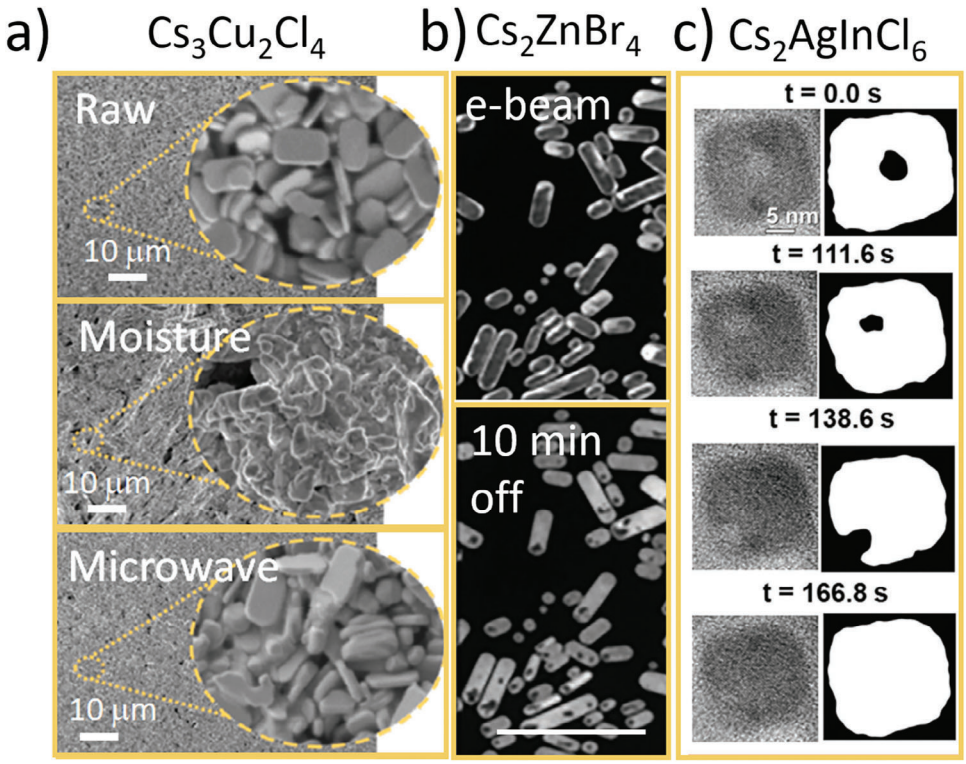

Figure 7. Healing in nanocrystals. a) Microwave-initiated healing in Cs_3CusCl_4 nanoparticles operating as a promising scintillator material. The nanoparticles are shown as synthesized (top), after decomposition due to moisture (middle), and after healing (bottom) by application of microwaves. (Reproduced with permission.[26n] Copyright 2022, Elsevier B.V.) b) Nanoshells formed from Cs_2ZnBr_4 nanocrystals by e-beam radiation (top) and recovered nanocrystals after switching off the beam for 10 min (bottom). (Reproduced with permission.[26p] Copyright 2023, Wiley VCH GmbH). c) Removal of a formed void in $Cs_2AgInCl_6$ colloidal colloidal nanocrystal after removal of its surface ligands by self-healing. (Reproduced with permission.[26r] Copyright 2021, Wiley VCH GmbH).

doping with various trivalent cations for luminescence enhancement by energy transfer processes.

5.1. Healing and Self-Healing in Lead-Free Perovskite Nanocrystals and Related Materials

As we have discussed the self-healing in lead-perovskites and its nanocrystals, it is worth discussing the same in lead-free nanocrystals, nanoparticles, and related materials which are of potential interest for X-ray scintillator applications. An interesting story about the healing of a scintillating microcrystalline material for high-resolution X-ray imaging is reported by Zhou et al.[26n] The material investigated here is $Cs_3Cu_2Cl_5$, which exhibits a relatively high photoluminescence quantum yield of ≈72% in films due to self-trapped excitons. These films have also been demonstrated for high-resolution X-ray imaging. However, the photoluminescence of the scintillating film decreases remarkably on time scales of days when the film is stored in an air environment maintained at a relative humidity between 40%–60%. The loss of luminescence was correlated by X-ray diffraction experiments to a decomposition of the $Cs_3Cu_2Cl_5$ into $CsCu_2Cl_3$ and CsCl. However, this reaction could be reversed by a 5-min treatment with microwave radiation, which restored the crystallites (**Figure** 7a) and their photoluminescence to more than 95% of its initial value. Zhou et al. suggest repeating this microwave treatment on a daily basis to maintain the good performance of the scintillating film. We think that the recovery of $Cs_3Cu_2Cl_5$ is indeed impressively shown, but the term self-healing is probably not justified here, but should rather be called microwave-induced healing. Similarly, Ju et al.[26o] demonstrated healing in melt-processable Cu(I) hybrid metal halides. In particular, $C_{12}H_{28}NCuCl_2$ and $C_{20}H_{48}N_2Cu_4Cl_6$ were shown to have melting temperatures of 86° and 122 °C, respectively, which are among the lowest melting temperatures of hybrid metal halides. Thus, these materials could be melt-processed into various shapes and films suitable for X-ray scintillation. $C_{12}H_{28}NCuCl_2$ has also been shown to have promising properties for X-ray imaging with a conversion efficiency of ≈36 000 photons MeV^{-1}. However, a disadvantage of these materials is that they oxidize, changing their color and losing their high luminescence properties. Thanks to the low melting temperature, a heat treatment at 120 °C for 15 min allows the materials to recrystallize, restoring almost 100% of their beneficial optical properties. The authors refer to this process as self-healing, but it is in fact a thermally driven recrystallization. While the 2 examples of scintillators can be healed by external stimuli, some nanoparticles or nanocrystals show healing without additional effort. A recent report describes in situ intrinsic self-healing of low-toxicity Cs_2ZnX_4 (X = Cl, Br) metal halide nanoparticles.[26p] For this purpose, the colloidally prepared nanoparticles were intentionally damaged by a focused beam of a scanning transmission

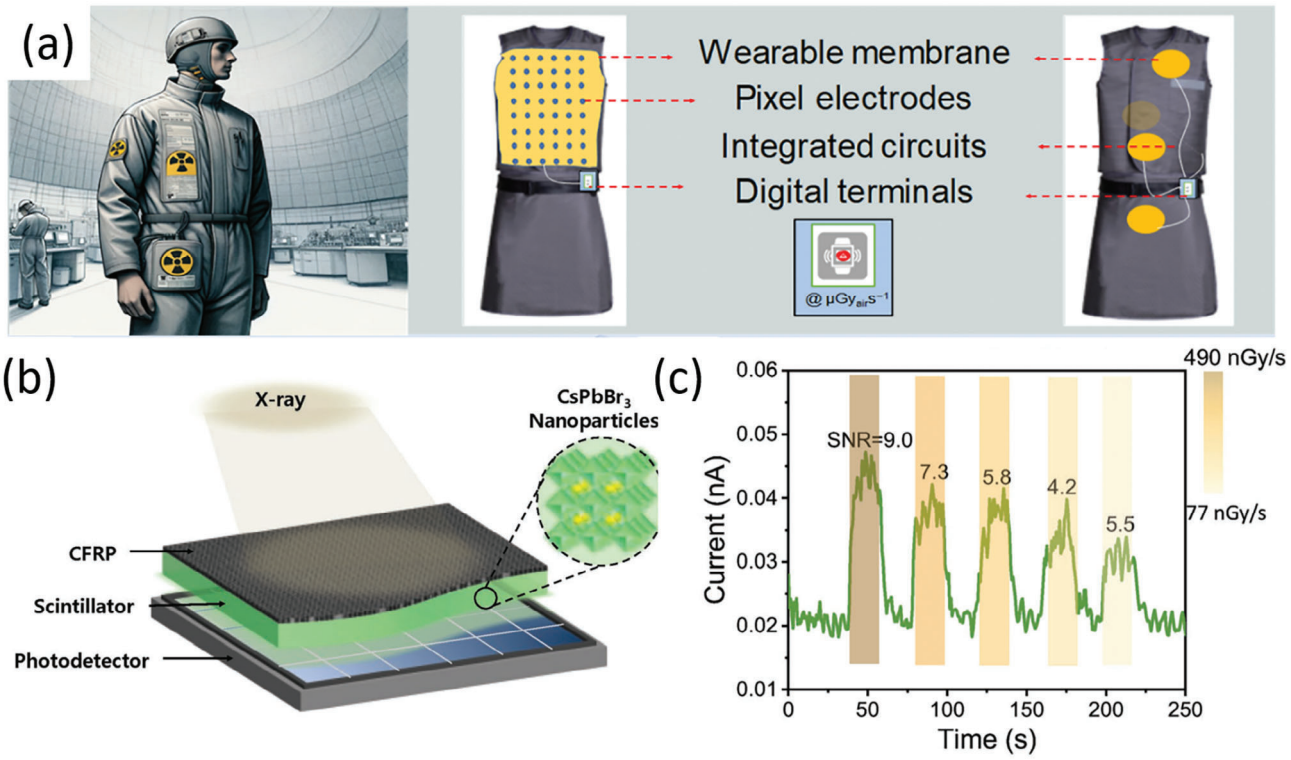

Figure 8. Flexible X-ray detectors. a) Potential use of flexible X-ray detectors as in-situ dose-meters integrated into the cloth of for instance the staff members in reactor buildings (Reproduced with permission.[27a] Copyright 2024, American Chemical Society). b) Integration of a flexible scintillator in an imaging device with an array of Si-based photodiodes covered by a carbon fiber reinforced polymer (CFRP) (Reproduced with permission.[20] Copyright 2018, Wiley VCH GmbH). c) Direct response of a flexible X-ray detector based on Eu^{2+} doped $MAPbBr_3$ nanocrystals incorporated into a highly ordered mesoporous silica material (Reproduced with permission.[27f] Copyright 2023, Wiley VCH GmbH).

electron microscope. This resulted in the transformation of, e.g., rod-like Cs_2ZnBr_4 into nanoshells. Turning off the electron beam for 10 min resulted in a retransformation of the nanoshells into almost completely filled nanorods, showing the original crystal structure (Figure 7b). Both the damage and the healing occurred at elevated temperatures caused by the electron beam heating the nanoparticles. However, here no additional stimulus was used to initiate the healing so that the observed process actually visualizes a true process of self-healing in nanoparticles or nanocrystals. This self-healing was made possible by small remnants of the original crystals inside the nanoshells, which seeded the regrowth of material inside the shells. It should also be noted that a potential application of these nanoparticles is X-ray scintillation, which is based on the broad luminescence of these materials between the ultraviolet and visible spectral range.[26q] However, the conversion yield demonstrated so far is not yet promising enough to rank these materials among the most promising scintillators without further improvements. Self-healing effects have also been demonstrated in double perovskite nanocrystals.[26r] Similar to the Cs_2ZnX_4, an electron beam of a transmission electron microscope has been used to provide damage during exposure in $Cs_2AgInCl_6$ and other related nanocrystals. In these nanocrystals, the electron beam induced the formation of voids that migrated into the interior of the nanocrystals. It was shown that the dynamics of these voids strongly depended on the presence or absence of surface ligands. Removal of the ligands allowed the voids to migrate to the surface of the nanocrystals and eventually be removed from the nanocrystal (Figure 7c). Thus, the in-situ observation of the void migration allowed us to visualize the complete self-healing of the nanocrystals. This observation was also supported by Monte Carlo simulations considering 2 terms: a surface effect depending on the ligand coverage and a self-healing term depending on the crystallization energy.[26r] While void formation and healing were also observed for $Cs_2Ag_{0.5}Na_{0.5}InCl_6$ and $Cs_2AgBiBr_6$, they were completely absent for $CsPbBr_3$, the workhorse for X-ray scintillation.

6. Halide Perovskite Nanocrystals in Flexible X-ray Detectors

If you look at the publications on X-ray detectors, you can see that an increasing number of scientists are working on flexible X-ray detectors. This presumably follows the efforts in the field of solar cells or light-emitting diodes, for which one can imagine useful applications for flexible components. But why do we need flexible X-ray detectors? An answer to this question is given in Ref. [27a]. In particular, it mentions dosimeters that are integrated into the clothing of specialized personnel working in reactor buildings, for example (**Figure 8a**). This would consist of a wearable membrane with pixel electrodes connected to readout electronics, which may transmit digitized signals wirelessly to a local data network. Flexible electronic components are often

very thin in order to achieve the desired flexibility. However, this is in stark contrast to the requirements of medical X-ray diagnostics, which aims to minimize the necessary X-ray doses for patients. For this reason, imaging X-ray detectors must have sufficient thickness to ensure that as few X-ray photons as possible pass through the X-ray detector unused.

Therefore, compromises regarding the thickness of the X-ray absorbing layer are not acceptable, at least for medical X-ray applications, and compromises that are usually made to make X-ray detectors flexible are not acceptable. X-ray detectors based on nanocrystals embedded in a polymer matrix are an exception. Since the flexibility is guaranteed by the matrix and the nanoscale-embedded quantum dots or nanocrystals do not restrict it. Therefore, most flexible X-ray detectors with sufficiently high absorption properties, which are conceivable for medical applications, are actually always based on nanoparticles. Of course, these nanoparticle-based flexible scintillators can only realize their full potential if they are coupled with a flexible photodetector array, e.g. made of organic semiconductors. There is already a wonderful review on perovskite nanocrystal-based scintillators for X-ray applications by Wang et al.[27b] In this review, all important work based on lead-based and lead-free nanocrystal scintillators up to the year 2022 is adequately described. They classify one of the first-ever demonstrated perovskite nanocrystal scintillators by Heo et al.[20] as flexible, because the X-ray converting layer was made from a solution of $CsPbBr_3$ nanocrystals in methyl methacrylate (MMA) and a photoinitiator. In the end, however, this layer was integrated into a close-to commercial detector package with a pixelated CMOS photodiode array, which of course took away the flexible properties of the whole setup (Figure 8b). Nevertheless, this paper by Heo et al.[20] was an important milestone for all further developments of flexible scintillators, which could eventually replace conventional materials because they allow a higher conversion rate or a higher lateral resolution.

For flexible scintillators, of course, what we had already stated for other scintillators remains true: it is important to avoid self-absorption, which can be achieved by a large Stokes shift of the luminescence, in flexible detectors, for example, by incorporating Mn into the perovskite structure[27d] or via the use of Cu-based perovskites which show emission of self-trapped excitons.[27e] Another important advantage of flexible scintillators is that they image non-planar objects more accurately than is possible with planar scintillators.[27b] We would like to add to the review by Wang et al.[27b] that it is clear that colloidal nanocrystals are very well suited for scintillator applications due to their sometimes high luminescence yield, but that they can also be used for direct conversion in flexible components. The latter was recently demonstrated with Eu^{2+} doped $MAPbBr_3$ nanocrystals embedded in SBA-15, a highly ordered mesoporous silica material.[27f] In these composites, the SBA-15 mainly helps the $MAPbBr_3$ nanocrystals to achieve higher stability. However, if this composite is combined with flexible styrene-ethylene-butylene-styrene (SEBS) substrates, on which lateral gold contacts have also been applied, photocurrents can also be measured. At a really low dark current of ≈10 pA, the photoconductors showed a remarkable conversion capacity of ≈7600 $\mu C Gy_{air}^{-1} cm^{-2}$ at an applied voltage of 100 V. (Figure 8c). Finally, it should be mentioned that in addition to nanocrystals, larger crystallites are also suitable for the development of flexible X-ray detectors. This brings us back to the work of Liu et al.[27a] in which a completely metal-free flexible perovskite ($MDABCO\text{-}NH_4I_3$), MDABCO = methyl-N′-diazabicyclo[2.2.2] octonium, was used to incorporate it into a flexible porous nylon membrane. (Figure 8c). Lateral contacts were also applied to this membrane so that photocurrents could be measured under X-ray excitation, with a sensitivity of 6522 $\mu C Gy_{air}^{-1} cm^{-2}$ and a low detection limit of 77 $nGy_{air} s^{-1}$, which is a good value for a biocompatible X-ray gene detector. This work also shows that there are other materials besides nanocrystalline scintillators for which it would be interesting to produce them in nanocrystalline form in the future, which will be discussed in the next chapter.

7. Promising Halide Perovskite Materials for Nanocrystal Scintillators

As exemplified by the CAMBIC story and other double perovskites discussed in Chapter 5, the development of perovskite scintillators with significant Stokes shift to avoid self-absorption in thick films has just begun. In our opinion, this research direction still has a high potential to improve also NC systems. A perspective for NCs is the development of microcrystalline powders, which, like nanocrystals, are also synthesized in solution by a bottom-up method. Ligands are not used, so there is no precise control over the size of the crystals, which do not exhibit colloidal stability even when dispersed. Nevertheless, these materials provide valuable clues for the further development of nanocrystalline inks for large-area printing of scintillators. For the synthesis of nanocrystals, materials with promising properties, such as MC powder, should be preferred. Promising microcrystalline materials besides CANBIC are cesium-hafnium,[28a,f] cesium-zirconium,[28b] rubidium-copper,[28c] cesium-antimony,[28d] cesium-cadmium,[28e] potassium-copper,[28g] methylammonium-indium,[28h] etc. It remains a challenge to synthesize these materials colloidally, e.g. by controlling growth and enhancing nucleation.

Encouraging microcrystals of Cs_2HfCl_6 were synthesized. A co-precipitation method was used at room temperature and the resulting powder was spread over a substrate using a doctor blade. The distributed powder was formed with a press into a more or less homogeneous film, which was tested as a scintillator as described in Ref. [28f]. These scintillators are stable in an ambient atmosphere and do not show any significant degradation up to a radiation dose of up to ten Gray. The emission shows a Stokes shift of ≈2.75 eV with respect to the absorption edge. The comparatively low light yield of 21 700 photons/MeV is due to the blue color of the emission. This value could probably be further increased by a suitable wavelength shifter. A typical solvothermal approach to the synthesis of tellurium-activated Cs_2HfCl_6 microcrystals in the form of hexaprisms[28a] (**Figure 9a**) resulted in a yellow RL emission, providing excellent scintillation parameters such as 76 194 photons MeV^{-1} and a detection limit of 36 $nGy\ s^{-1}$. A similar solvothermal approach, in this case, lutecium-doped Cs_2ZrCl_6 (Figure 9b), provided MCs with an even lower detection limit of 15.8 $nGy\ s^{-1}$ and a somewhat better light yield of 94 190 photons MeV^{-1}, with 2.2 eV Stokes shift originating from a singlet-triplet transition. Here, a decent Stokes shift (Figure 9c)

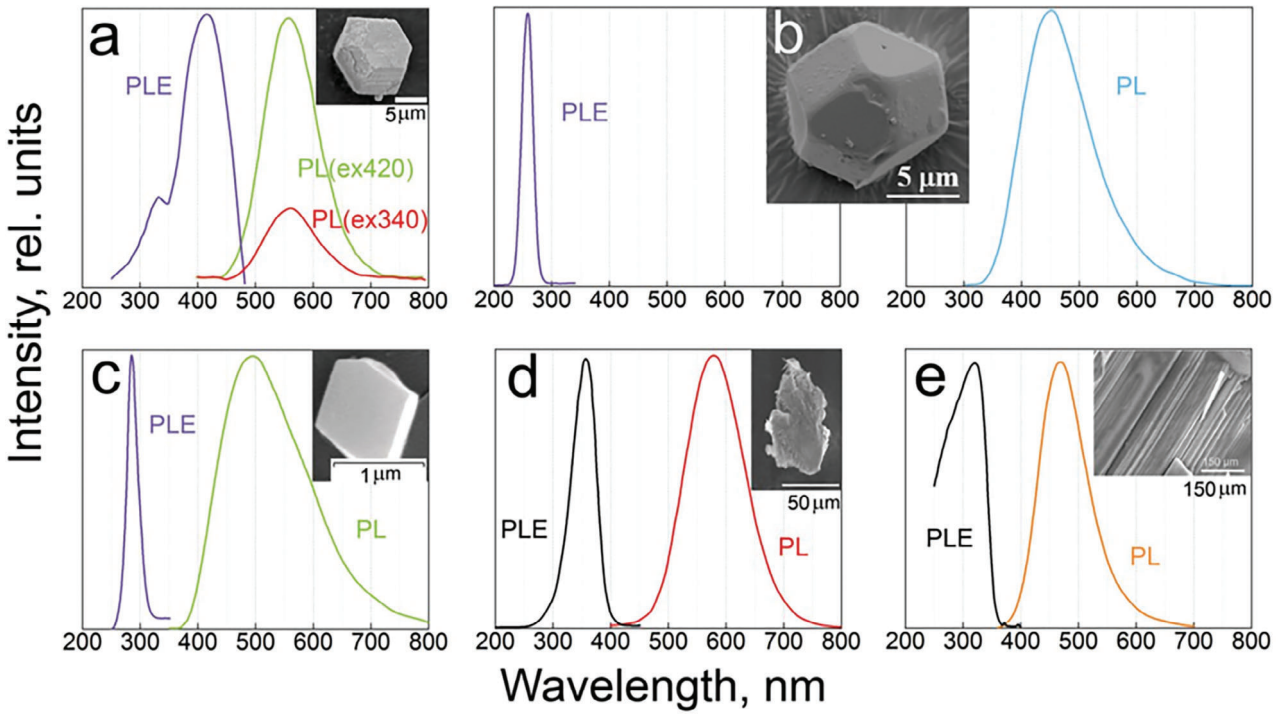

Figure 9. Comparison of the Stokes shifts in diverse lead-free HP MCs. The insets show the shapes of the HP MCs. In particular, the following materials are shown: a) Cs_2HfCl_6:Te^{4+} (Reproduced with permission.[28a] Copyright 2022, Royal Society of Chemistry); b) Cs_2ZrCl_6: Lu^{3+} (Reproduced with permission.[28b] Copyright 2022, American Chemical Society); c) $Cs_2CdBr_2Cl_2$: Mn^{2+} (Reproduced with permission.[28e] Copyright 2023, Wiley VCH GmbH); d) $(C_8H_{17}NH_3)_2SnBr_4$ (Reproduced with permission.[29a] Copyright 2020, American Chemical Society); e) $(C_8H_{17}NH_3)_2Cu_2Br_4$ (Reproduced with permission.[29b] Copyright 2022, Wiley VCH GmbH).

was realized via emission generated solely by 4T1→6A1 transitions in the divalent manganese ions, with the HP host lattice causing the optical absorption in this material.[28e]

Cadmium-free HP MCs with a similar strategy of Stokes shift engineering by manganese incorporation were presented in Ref. [28i] for the cesium-silver-indium double perovskite. In this material, the maximum photoluminescence intensity was achieved with an Mn concentration of 0.9%, providing a long decay time in the ms range. Mainly for high-temperature applications, Cu-based perovskites were tested in Ref. [28j] Among several halide compositions, $Cs_5Cu_3Cl_6I_2$ MCs synthesized at room temperature by an antisolvent method showed the best performance. Such submicron diameter MCs encapsulated in PDMS yield up to 59 700 photons MeV^{-1} and stable scintillating properties up to absorbed doses of a few grays. Typically, SC HP scintillators exhibit performance parameters close to those of MC powders. For example, mm-sized Rb_2CuBr_3 SCs grown from a slowly cooled solution showed excellent scintillator performance figures (see Ref. [28c] in Table 1).

K_2CuBr_3 SCs scintillators emit in the violet spectral region, with a decent light yield of 23 806 photons MeV^{-1} and a Stokes shift of 0.83 eV.[28g] As a potential drawback, the authors discussed that the long half-life radioactive isotope of natural potassium, which provides mutual β and γ emissions, even when incorporated into the HP structures, could affect any low dose measurements. However, for the demonstrated detector, the detection limit above the noise level was found to be higher than what could be attributed to the effects of natural radioactivity. Of course, this problem is probably also valid for the natural rubidium of Ref. [28c], which contains about a quarter of the γ active isotopes. However, its half-life is even longer than that of potassium ($\approx 5 \times 10^{10}$ years), so its effect on the detection limit is even smaller. To convert the SCs into MC powders, mechanical milling approaches have been routinely applied in scintillator technology, resulting in submicron particle sizes even in the worst cases.[28e,k] Milling can be applied to various types of SC HPs, including those containing bulky alkylamine monocations to obtain layered materials. Examples of such materials include octylammonium tin HP, whose crystals exhibit significant Stokes shifts (see Figure 9d) and can withstand up to 10 mGy s^{-1} dose rates.[29a] Such layered materials, including $(C_8H_{17}NH_3)_2Cu_2Br_4$, are desirable because they facilitate top-down techniques. Exfoliation by mechanical, tape, or ultrasound-assisted approaches is particularly successful due to its micaceous structure, as shown in the cross-section in Figure 9e.[29b] The octylammonium copper MC HP powders are reabsorption-free. Wafers made from these powders by cold pressing and sintering have high sensitivity and remarkable light yield (Table 1).

The exfoliation would allow a much more precise size control of the MCs or NCs, related to the number of elemental HP layers separated by spacious amine ions, either of aromatic nature or at least with a carbon chain length of butyl.[13d,29c] Lead-free MC scintillators can provide near-unity PLQY paired with other advantages over their LHP counterparts, namely: i) more freedom in Stokes shift tuning via an expanded combination of elemental compositions also with respect to their incorporated

activators; ii) less complicated synthesis protocols without surface stabilization by surfacing ligands; ii) native moisture and humidity friendliness due to the absence of Pb^{2+} ions readily soluble in water;[24b] iv) enhanced radiation stability due to the absence of Pb^{2+} ion disproportionation phenomena, (i.e., the detectors will not be degraded by partial conversion to metallic lead);[20b] v) although some parts of medical X-ray diagnostics are currently exempted from the RoHS restriction,[30] lead-free and cadmium-free HP will also not be restricted by the upcoming updates of the RoHS versions.

To provide a concise overview, we have summarized the current achievements of HP NCs (with an illustrative comparison of their desired MC and SC counterparts) for X-ray detection and their main scintillation properties in Table 1. Finally, we would like to note that as a result of the success of perovskite-like materials in nanocrystalline and microcrystalline form for high-energy radiation detection, we also see them as a stimulus for other luminescent materials to be used for X-ray detection. Examples of new developments are aggregation-induced emission luminescent metal-organic frameworks embedded in a polymer matrix with high spatial resolution.[31a] Unfortunately, the test conditions of this material have not been described, especially regarding the used X-ray energy range. Another example with a relatively high scintillator light yield of 43 744 photons MeV^{-1} is given by a 0D hybrid copper halide in Ref. [31b], which in turn is outperformed by 0D hybrid copper bromides in the form of single crystals with 91 300 photons MeV^{-1}. Thus, Cu(I)-containing fluorescent complexes have been combined with $CsPbBr_3$ in a polymer matrix to act as down-converters to achieve maximum radioluminescence without reabsorption.[31c] And recently, even metal nanoclusters have been assembled to provide a new class of environmentally friendly scintillators that exhibit aggregation-induced emission enhancement and high phosphorescence quantum yields.[31d] These nanoclusters assemble into superparticles that can be dispersed in appropriate solvents, such as the colloidal nanocrystals discussed above. After film formation on a filter membrane, even these nanocluster superparticles provide high-resolution X-ray images with a decent light yield of ≈15 000 photons MeV^{-1} higher than commercial $Bi_4Ge_3O_{12}$.[31e]

In view of the parameters provided in Table 1 exhibiting light yields and detection limits, which are very competitive to those of commercial scintillators, it is already difficult to imagine what else should be developed and why these materials are not yet implemented. The values are reproduced as given in the referenced publications, but these values still have to be taken with some care. Indeed, it is also necessary to look at how these values were measured and how they could be compared to each other. Therefore, instead of simply providing the light yield and detection limit in Table 1 there is also the range of X-ray energies given, for which the scintillators were tested, in order to judge if these detectors would be promising for any medical applications. Furthermore, some details should be explained. For a medical detector, for instance, the light yield is an important number provided as a ratio between the number of emitted photons per energy of the incident photons. However, the maximum number in Table 1 of 177 000 photons MeV^{-1} was measured in Ref. [20f] as the number of photons per total energy of incident photons, which thus provides a higher number. What is also suspicious is that the numbers for Ref. [20f,21a], both obtained for very similar $CsPbBr_3$ nanocrystals are completely different. For both references, the nanocrystals were tested in a PMMA matrix for scintillation purposes. However, the light yield was measured for completely different sample structures. Indeed in[20f] the nanocrystals were rather highly diluted in the PMMA matrix, which indeed will greatly avoid reabsorption, whereas in[21a] the yield was measured in uniformly compacted nanocrystal powders. The Cs_2ZrCl_6:Lu^{3+} in Ref. [28b] provides the light yield for a pressed pellet of scintillator material and obtains a high value for the scintillation light yield of 94 190 photons MeV^{-1}, which is enabled by the large Stokes shift in this material avoiding any reabsorption in a densely bulk material. While this part is very promising, the scintillator's spatial resolution was measured in films of the perovskite in an epoxy matrix. The spatial resolution depended strongly on film thickness; all of them were too thin to enable the high light yield as measured in the pressed pellet. The reason for the thin film approach here is the scattering caused by the microcrystallinity of the perovskites. Thus, in conclusion, we can say that for actual scintillating devices, there is still room for improvements, and certainly, all parameters provided for a novel scintillator should be provided by using the same sample structure and not the yield for one and the imaging for another. Even though this possibly allows showing the potential for a novel material, it is highly misleading for any user interested in applying a novel scintillator structure and for any fair comparison of devices.

8. Conclusions and Outlook

In this review, we have drawn several conclusions and challenges for HP NCs concerning their application for the detection of indirect X-rays. The applicability of HP NCs for down-conversion of ionizing radiation has not yet achieved such attraction as their bulk SC and MC counterparts, even though HP NCs are advantageous with respect to their processability into hybrid assemblies, into thick and homogenous films or also in their integration on pixelated photodetector arrays by methods based on deposition of stable colloidal solutions by several printing techniques. The light yield summarized in Table 1 highlights the promising properties of NCs, providing, for instance, light yields up to values of 177 000 photons MeV^{-1}, achieved for $CsPbBr_3$ NCs embedded in a PMMA matrix. Regarding detection, again $CsPbBr_3$ competes very well with all other materials in this review, so the cesium lead tribromide NCs can be seen as the best workhorse for nanocrystalline solution-processed HP materials. In particular, it is clearly outperforming all organic-inorganic hybrid perovskites that were reported for the same applications, which is perhaps opposite to single crystalline lead HPs scintillators, wherein alkylammonium-based HP dominates the field, specifically as low-temperature scitillators.[31f] The reasons are the tiny Stokes shifts routinely increased by dopant modulation for LHP NCs. For the pristine cesium lead bromide NCs, this drawback is neutralized by a negative thermal quenching luminescence mechanism.[17b]. Disadvantages of the LHP NCs are potential ambient and radiation instabilities, which are severely improved by protection strategies such as ligand exchanges,[25b] shell growth,[14b] or incorporation into organic frameworks[20d]. Another strategy to improve NC-based scintillators is based on hybrid approaches that combine functionalities. For example, LHP NCs are applied as absorbers combined with bright

organic dyes acting as emitters. Embedding in intrinsic or extrinsic protective matrixes and incorporating appropriate emission activators also improve light yields, detection limit, and lateral resolution.[31f] The lead-free HP NCs prepared by bottom-up approaches are still far less developed than a larger variety of lead-free HP MCs and SCs, despite their potential advantages such as nontoxicity and improved environmental stability. Among various approaches, competitive values for the figures of merit for scintillators were achieved only for cesium copper and scarce lanthanide-based colloidal HP NCs. To make such NCs suitable for scintillation purposes, applying conventional surface ligands of variable strength, being over-successful for common covalently bound semiconductor NC materials failed. Advanced ligands approached here to improve the situation are of ionic species,[20b,25b] preventing the cations of the perovskites from escaping from the NCs by forming confining core-shell structures, such as they have already been engineered for some LHP NCs.[14b] NCs grown in intrinsic or glass matrixes also solve this problem, but they are rather unprocessable by subsequent film deposition methods, just as SC materials are. To obtain an impetus for the development of lead-free HP NCs we suggest thoroughly paying attention to the recent developments in MC HPs prepared by both top-down and bottom-up approaches. As MCs have a tremendously lower surface-to-volume ratio, they do not urgently require surface passivation and protection measures, as the concentration of surface defects is essentially lower. Time-limited stability in typical dispersions still allows the application of some conventional deposition techniques from solutions to achieve scintillating films of satisfactory roughness and optical quality, at least when combined with subsequent improvements, for instance, by using pressuring plates. Adoption of these successful materials to the NC form still represents challenges, especially again in maintaining sufficient surface passivation by shell growth, encapsulation in crystalline matrix, glasses or polymers, as has been demonstrated for the showcase example of $CsPbBr_3$, to obtain highly functional, but also environmentally stable and non-toxic scintillator materials for future large scale applications in the various fields of X-ray applications. Following the development path for nanocrystalline materials by first checking the microcrystalline counterparts could considerably speed up the nanocrystal development. Especially because the bottom-up and top-down syntheses of microcrystals are technically often rather simple, so they are suitable to be performed by robot-assisted procedures. Thus, fully automated high throughput experiments could be performed for the screening of material candidates. These automated preselection experiments will provide the target compositions for further synthetic developments of nanocrystals by more elaborate experiments requiring more complicated procedures, which are still best performed by experienced man-power, finally to obtain nanocrystal-based inks for the large-scale printing of high-performance X-ray scintillating screens.

Acknowledgements

The authors gratefully acknowledge that this work was funded by the Volkswagen Foundation and partly by the Deutsche Forschungsgemeinschaft (DFG), project No. GRK2495/J.

Open access funding enabled and organized by Projekt DEAL.

Conflict of Interest

The authors declare no conflict of interest.

Keywords

halide perovskites, lead-free, nanocrystals, scintillators, Stokes shift

Received: January 29, 2024
Revised: April 25, 2024
Published online: May 26, 2024

[1] a) S. S. Yu, H. R. Zhao, W. Xu, H. Zhang, H. B. Duan, *Front. Electron. Mater.* **2022**, *2*, 891983; b) C. Perumal Veeramalai, S. Feng, X. Zhang, S. Pammi, V. Pecunia, C. Li, *Photon. Res.* **2021**, *9*, 968; c) H. Choi, S. Seo, J.-H. Kim, J.-H. Lee, S. Kim, G. Piao, H. Park, K. Lee, S. Lee, *J. Mater. Chem. A.* **2021**, *9*, 22291; d) L. Zhang, J. Miao, J. Li, Q. Li, *Adv. Funct. Mater.* **2020**, *30*, 2003653; e) A. K. Jena, A. Kulkarni, T. Miyasaka, *Chem. Rev.* **2019**, *119*, 3036; f) P. Roy, A. Ghosh, F. Barclay, A. Khare, E. Cuce, *Coatings* **2022**, *12*, 1089.

[2] a) H. Jiang, S. Cui, Y. Chen, H. Zhong, *Nano Select* **2021**, *2*, 2040; b) F. Temerov, Y. Baghdadi, E. Rattner, S. Eslava, *ACS Appl. Energy Mater.* **2022**, *5*, 14605; c) Z. Song, J. Zhao, Q. Liu, *Inorg. Chem. Front.* **2019**, *6*, 2969.

[3] a) X. He, Y. Deng, D. Ouyang, N. Zhang, J. Wang, A. A. Murthy, I. Spanopoulos, S. M. Islam, Q. Tu, G. Xing, Y. Li, V. P. Dravid, T. Zhai, *Chem. Rev.* **2023**, *123*, 1207; b) S. Gull, M. H. Jamil, X. Zhang, H.-S. Kwok, G. Li, *Chem. Open* **2022**, *11*, e202100285.

[4] a) P. Lecoq, *Nucl. Instr. Meth. Phys. Res. A* **2016**, *809*, 130; b) J. C. Yanch, R. H. Behrman, M. J. Hendricks, J. H. McCall, *Radiology* **2009**, *252*, 128; c) T. Stalbaum, D. Boyd, M. Weil, H. Chen, M. Plies, S. Song, V. Ziskin, M. Bazalova-Carter, J. Boone, M. Daly, L. Partain, *Proc. SPIE* **2020**, *11312*, 113123I; d) K. Moshkbar-Bakhshayesh, H. Afarideh, R. Azimirad, *Rad. Phys. Chem.* **2023**, *212*, 111180.

[5] a) T. J. Hajagos, C. Liu, N. J. Cherepy, Q. Pei, *Adv. Mater.* **2018**, *30*, 1706956; b) M. Koshimizu, *Jpn. J. Appl. Phys.* **2023**, *62*, 010503; c) M. Nikl, *Meas. Sci. Technol.* **2006**, *17*, R37; d) C. Ronda, H. Wieczorek, V. Khanin, P. Rodnyi, *ECS J. Solid State Sci. Techn.* **2015**, *5*, R3121; e) C. Dujardin, E. Auffray, E. Bourret-Courchesne, P. Dorenbos, P. Lecoq, M. Nikl, A. N. Vasil'ev, A. Yoshikawa, R.-Y. Zhu, *IEEE Trans. Nucl. Sci.* **2018**, *65*, 1977.

[6] a) W. C. Röntgen, *Science* **1896**, *3*, 227 b) W. C. Röntgen, *Ann. Phys.* **1898**, *300*, 18; c) Z. Lin, S. Lv, Z. Yang, J. Qiu, S. Zhou, *Adv. Sci.* **2022**, *9*, 2102439.

[7] a) Y. Haruta, M. Kawakami, Y. Nakano, S. Kundu, S. Wada, T. Ikenoue, M. Miyake, T. Hirato, M. I. Saidaminov, *Chem. Mater.* **2022**, *34*, 5323; b) H. Wu, Y. Ge, G. Niu, J. Tang, *Matter* **2021**, *4*, 144; c) N. J. Jeon, J. M. Cho, J.-K. Lee, *Progr. Med. Phys.* **2022**, *33*, 11; d) S. Li, X. Xie, J. Xiong, F. Wang, J. Liu, M. Jiang, *Crystals* **2022**, *12*, 1563; e) F. Liu, R. Wu, J. Wei, W. Nie, A. D. Mohite, S. Brovelli, L. Manna, H. Li, *ACS Energy Lett.* **2022**, *7*, 1066; f) Y. Zhou, J. Chen, O. M. Bakr, O. F. Mohammed, *ACS Energy Lett.* **2021**, *6*, 739; g) L. Lu, M. Sun, T. Wu, Q. Lu, B. Chen, B. Huang, *Nanoscale Adv.* **2022**, *4*, 680.

[8] a) W. Ma, Y. Su, Q. Zhang, C. Deng, L. Pasquali, W. Zhu, Y. Tian, P. Ran, Z. Chen, G. Yang, G. Liang, T. Liu, H. Zhu, P. Huang, H. Zhong, K. Wang, S. Peng, J. Xia, H. Liu, X. Liu, Y. M. Yang, *Nature Mater* **2022**, *21*, 210; b) M. J. Berger, J. H. Hubbell, S. M. Seltzer, J. Chang, J. S. Coursey, R. Sukumar, D. S. Zucker, K. Olsen, *XCOM: Photon Cross Sect. Database* **2010**, 87, http://doi.org/10.18434/T48G6X.

[9] L. Chouhan, S. Ghimire, C. Subrahmanyam, T. Miyasaka, V. Biju, *Chem. Soc. Rev.* **2020**, *49*, 2869.

[10] M. Nikl, A. Yoshikawa, *Adv. Optical Mater.* **2015**, *3*, 463.

[11] a) M. Nikl, K. Nitsch, K. Polak, G. P. Pazzi, P. Fabeni, D. S. Citrin, M. Gurioli, *Phys. Rev. B* **1995**, *51*, 5192; b) M. Nikl, K. Nitsch, K. Polák, E. Mihókova, S. Zazubovich, G. P. Pazzi, P. Fabeni, L. Salvini, R. Aceves, M. Barbosa-Flores, R. P Salas, M. Gurioli, A. Scacco, *J Luminesc.* **1997**, *72–74*, 377; c) M. Nikl, K. Nitsch, E. Mihóková, K. Polák, P. Fabeni, G. P Pazzi, M. Gurioli, S. Santucci, R. Phani, A. Scacco, F. Somma, *Phys. E* **1999**, *4*, 323; d) A. Voloshinovskii, S. Myagkota, A. Gloskovskii, V. Gaba, *J. Phys. Cond. Matter* **2001**, *13*, 8207; e) M. Nikl, K. Nitsch, J. Chval, F. Somma, A. R. Phani, S. Santucci, C. Giampaolo, P. Fabeni, G. P. Pazzi, X. Q. Feng, *J. Phys. Cond. Matter* **2000**, *2*, 1939.

[12] a) L. Protesescu, S. Yakunin, M. I. Bodnarchuk, F. Krieg, R. Caputo, C. H. Hendon, R. X. Yang, A. Walsh, M. V. Kovalenko, *Nano Lett.* **2015**, *15*, 3692; b) D. Zhang, S. W. Eaton, Y. Yu, L. Dou, P. Yang, *J. Am. Chem. Soc.* **2015**, *137*, 9230; c) G. Nedelcu, L. Protesescu, S. Yakunin, M. I. Bodnarchuk, M. J. Grotevent, M. V. Kovalenko, *Nano Lett.* **2015**, *15*, 5635; d) Q. A. Akkerman, V. D'Innocenzo, S. Accornero, A. Scarpellini, A. Petrozza, M. Prato, L. Manna, *J. Am. Chem. Soc.* **2015**, *137*, 10276.

[13] a) A. Dey, J. Ye, A. De, E. Debroye, S. K. Ha, E. Bladt, A. S. Kshirsagar, Z. Wang, J. Yin, Y. Wang, L. N. Quan, F. Yan, M. Gao, X. Li, J. Shamsi, T. Debnath, M. Cao, M. A. Scheel, S. Kumar, J. A. Steele, M. Gerhard, L. Chouhan, K. Xu, X.-G. Wu, Y. Li, Y. Zhang, A. Dutta, C. Han, I. Vincon, A. L. Rogach, et al., *ACS Nano* **2021**, *15*, 10775; b) K. Hills-Kimball, H. Yang, T. Cai, J. Wang, O. Chen, *Adv. Sci.* **2021**, *8*, 2100214; c) F. Di Stasio, S. Christodoulou, N. Huo, G. Konstantatos, *Chem. Mater.* **2017**, *29*, 7663; d) B. Dhanabalan, A. Castelli, M. Palei, D. Spirito, L. Manna, R. Krahne, M. Arciniegas, *Nanoscale* **2019**, *11*, 8334.

[14] a) N. Fiuza-Maneiro, K. Sun, I. López-Fernández, S. Gómez-Graña, P. Müller-Buschbaum, L. Polavarapu, *ACS Energy Lett.* **2023**, *8*, 1152; b) Q. Zhang, M. He, Q. Wan, W. Zheng, M. Liu, C. Zhang, X. Liao, W. Zhan, L. Kong, X. Guo, L. Li, *Chem. Sci.* **2022**, *13*, 3719; c) B. Zhang, L. Goldoni, C. Lambruschini, L. Moni, M. Imran, A. Pianetti, V. Pinchetti, S. Brovelli, L. De Trizio, L. Manna, *Nano Lett.* **2020**, *20*, 8847; d) C. Ren, Z. Li, L. Huang, X. Xiong, Z. Nie, Y. Yang, W. Zhu, W. Yang, L. Wang, *Nanoscale* **2022**, *14*, 4216.

[15] a) T. C. Jellicoe, J. M. Richter, H. F. J. Glass, M. Tabachnyk, R. Brady, S. E. Dutton, A. Rao, R. H. Friend, D. Credgington, N. C. Greenham, M. L. Böhm, *J. Am. Chem. Soc.* **2016**, *138*, 2941; b) S. A. Khan, N. Z. Khan, M. Sohail, M. Runowski, X. Xu, S. Agathopoulos, *Mater. Today Phys.* **2023**, *34*, 101079; c) C. K. Ng, C. Wang, J. J. Jasieniak, *Langmuir* **2019**, *35*, 11609; d) J. Huang, T. Lei, M. Siron, Y. Zhang, S. Yu, F. Seeler, A. Dehestani, L. N. Quan, K. Schierle-Arndt, P. Yang, *Nano Lett.* **2020**, *20*, 3734; e) C. Wang, J. Xiao, Z. Yan, X. Niu, T. Lin, Y. Zhou, J. Li, X. Han, *Nano Res.* **2023**, *16*, 1703; f) S. Wang, W. Jiang, W. Cui, W. Jiang, M. Zhao, J. Sun, B. Liu, X. Lai, K. Shi, K. Pan, *Adv. Optical Mater.* **2023**, *11*, 2202745; g) Z. Liu, J. Zito, M. Ghini, L. Goldoni, M. Prato, H. B. Jalali, I. Infante, L. De Trizio, L. Manna, *Nano Lett.* **2022**, *22*, 8567; h) C. Wang, N. Zhao, H. Zhang, X. Zhang, X. H. Lin, H. Liu, F. Dang, W. Zhang, J. Sun, P. Chen, H. Chen, P. Han, P. Li, *ACS Sustainable Chem. Eng.* **2023**, *11*, 14659; i) P. Vashishtha, B. E. Griffith, Y. Fang, A. Jaiswal, G. V. Nutan, A. P. Bartok, T. White, J. V. Hanna, *J. Mater. Chem. A* **2022**, *10*, 3562; j) J. Nie, B. Zhou, S. Fang, Y. Wang, Y. Wang, B. Tian, H. Hu, H. Zhong, H. Li, Y. Shi, *Mater. Today Phys.* **2023**, *31*, 100992; k) X. Li, D. Wang, Y. Zhong, F. Jiang, D. Zhao, S. Sun, P. Lu, M. Lu, Z. Wang, Z. Wu, Y. Gao, Y. Zhang, W. W. Yu, X. Bai, *Adv. Sci.* **2023**, *10*, 2207571; l) H. Li, M. Zhang, Y. Li, X. Fu, J. Feng, H. Zhang, *Adv. Optical Mater.* **2023**, *11*, 2300429; m) P. Saghy, A. M. Brown, C. Chu, L. C. Dube, W. Zheng, J. R. Robinson, O. Chen, *Adv. Optical Mater.* **2023**, *11*, 2300277; n) H. Li, L. Tian, Z. Shi, Y. Li, C. Li, J. Feng, H. Zhang, *J. Mater. Chem. C* **2022**, *10*, 10609.

[16] V. M. Goldschmidt, *Naturwissen* **1926**, *14*, 477.

[17] a) H. Wu, J. Pi, D. Zhou, Q. Wang, Z. Long, J. Qiu, *Ceram. Int.* **2022**, *48*, 3383; b) F. Maddalena, A. Xie, X. Y. Chin, R. Begum, M. E. Witkowski, M. Makowski, B. Mahler, W. Drozdowski, S. V. Springham, R. S. Rawat, N. Mathews, C. Dujardin, M. D. Birowosuto, C. Dang, *J. Phys. Chem. C* **2021**, *125*, 14082.

[18] a) Y. Zhang, R. Sun, X. Ou, K. Fu, Q. Chen, Y. Ding, L.-J. Xu, L. Liu, Y. Han, A. V. Malko, X. Liu, H. Yang, O. M. Bakr, H. Liu, O. F. Mohammed, *ACS Nano* **2019**, *13*, 2520; b) S. Cho, S. Kim, J. Kim, Y. Jo, I. Ryu, S. Hong, J.-J. Lee, S : N. Cha, E. B. Nam, S. U. Lee, S. K. Noh, H. Kim, J. Kwak, H. Im, *Light Sci. Appl.* **2020**, *9*, 156; c) M. Liu, L. Huang, D. Yuan, Z. Li, Y. Teng, J. Zhang, S. Huang, B. Liu, *ACS Appl. Nano Mater.* **2023**, *6*, 370.

[19] J. Liu, X. Zheng, O. F. Mohammed, O. M. Bakr, *Acc. Chem. Res.* **2022**, *55*, 262.

[20] a) L. Yang, H. Zhang, M. Zhou, L. Zhao, W. Chen, T. Wang, X. Yu, D. Zhou, J. Qiu, X. Xu, *J. Phys. Chem. Lett.* **2020**, *11*, 9203; b) J. Wahl, P. Haizmann, C. Kirsch, R. Frecot, N. Mukharamova, D. Assalauova, Y. Y. Kim, I. Zaluzhnyy, T. Chassé, I. A. Vartanyants, H. Peisert, M. Scheele, *Phys. Chem. Chem. Phys.* **2022**, *24*, 10944; c) Z.-W. Lü, G.-X. Wei, H.-Q. Wang, Y. Guan, N. Jiang, Y.-Y. Liu, Z. Li, H. Qin, H.-Q. Liu, *Nucl. Sci. Techn.* **2022**, *33*, 98; d) Q. Chen, J. Wu, X. Ou, B. Huang, J. Almutlaq, A. A. Zhumekenov, X. Guan, S. Han, L. Liang, Z. Yi, J. Li, X. Xie, Y. Wang, Y. Li, D. Fan, D. B. L. Teh, A. H. All, O. F. Mohammed, O. M. Bakr, T. Wu, M. Bettinelli, H. Yang, W. Huang, X. Liu, *Nature* **2018**, *561*, 88; e) L. Xiang, Y. Wang, X. Liu, X. Huang, Z. Xin, Y. Xu, C. Liu, K. Wang, J. Chen, Y. Yang, *Flex. Print. Electron.* **2021**, *6*, 015008; f) J. H. Heo, D. H. Shin, J. K. Park, D. H. Kim, S. J. Lee, S. H. Im, *Adv. Mater.* **2018**, *30*, 1801743.

[21] a) M. L. Zaffalon, F. Cova, M. Liu, A. Cemmi, I. Di Sarcina, F. Rossi, F. Carulli, A. Erroi, C. Rodà, J. Perego, A. Comotti, M. Fasoli, F. Meinardi, L. Li, A. Vedda, S. Brovelli, *Nature Photon* **2022**, *16*, 860; b) D. R. Ceratti, Y. Rakita, L. Cremonesi, R. Tenne, V. Kalchenko, M. Elbaum, D. Oron, M. A. C. Potenza, G. Hodes, D. Cahen, *Adv. Mater.* **2018**, *30*, 1706273; c) K. Děcká, F. Pagano, I. Frank, N. Kratochwil, E. Mihóková, E. Auffray, V. Čuba, *J. Mater. Chem. C* **2022**, *10*, 12836; d) A. Magi, M. Koshimizu, A. Sato, Y. Fujimoto, S. Kishimoto, T. Yanagida, K. Asai, *Jpn. J. Appl. Phys.* **2022**, *61*, SB1036.

[22] a) J.-X. Wang, X. Wang, J. Yin, L. Gutiérrez-Arzaluz, T. He, C. Chen, Y. Han, Y. Zhang, O. M. Bakr, M. Eddaoudi, O. F. Mohammed, *ACS Energy Lett.* **2022**, *7*, 10; b) M. Gandini, I. Villa, M. Beretta, C. Gotti, M. Imran, F. Carulli, E. Fantuzzi, M. Sassi, M. Zaffalon, C. Brofferio, L. Manna, L. Beverina, A. Vedda, M. Fasoli, L. Gironi, S. Brovelli, *Nature Nanotechn.* **2020**, *15*, 462; c) W. Chen, X. Tang, Y. Liu, Z. Xu, Y. Zicheng, Z. Zhang, K. Liu, *Int. J. Energy Res.* **2019**, *43*, 4520.

[23] a) Y. Xu, X. Li, M. Xia, X. Zhang, *J. Lumin.* **2022**, *248*, 118924; b) Q. Xu, J. Wang, W. Shao, X. Ouyang, X. Wang, X. Zhang, Y. Guoa, X. Ouyang, *Nanoscale* **2020**, *12*, 9727; c) R. T. Williams, W. W. Wolszczak, X. Yan, D. L. Carroll, *ACS Nano* **2020**, *14*, 5161; d) Z. Zhang, H. Dierks, N. Lamers, C. Sun, K. Nováková, C. Hetherington, I. G. Scheblykin, J. Wallentin, *ACS Appl. Nano Mater.* **2022**, *5*, 881; e) H. Dierks, Z. Zhang, N. Lamers, J. Wallentin, *Nano Res.* **2023**, *6*, 1084.

[24] a) B. Zhang, K. Zhang, L. Li, C. Xu, R. Wang, C. Wang, J. Yang, Y. Yang, *J. Alloys Comp.* **2021**, *874*, 159962; b) P. Aryal, H. J. Kim, S. Saha, J. Cho, A. V. Ntarisa, S. Kothan, *J. Alloys Comp.* **2021**, *866*, 158974; c) Y. Ye, W. Zhang, Z. Zhao, J. Wang, C. Liu, Z. Deng, X. Zhao, J. Han, *Adv. Optical Mater.* **2019**, *7*, 1801663; d) Y. Tong, Q. Wang, H. Yang, X. Liu, E. Mei, X. Liang, Z. Zhang, W. Xiang, *Photon. Res.* **2021**, *9*, 2369; e) W. Ma, T. Jiang, Z. Yang, H. Zhang, Y. Su, Z. Chen, X. Chen, Y. Ma, W. Zhu, X. Yu, H. Zhu, J. Qiu, X. Liu, X. Xu, Y. Yang, *Adv. Sci.* **2021**, *8*, 2003728; f) H. Zhang, Z. Yang, M. Zhou, L. Zhao, T. Jiang, H. Yang, X. Yu, J. Qiu, Y. Yang, X. Xu, *Adv. Mater.* **2021**, *33*, 2102529; g) Y. Xu, X. Zhao, M. Xia, X. Zhang, *J. Mater. Chem. C* **2021**, *9*, 5452; h) L. Niu, S. Wang, Z. Sui, Y. Song, L. Zhao, L. Liu, J. Ren, J. Zhang, *Opt. Lett.* **2021**, *46*, 3448.

[25] a) C. Wang, H. Lin, Z. Zhang, Z. Qiu, H. Yang, Y. Cheng, J. Xu, X. Xiang, L. Zhang, Y. Wang, *J. Europ. Ceram. Soc.* **2020**, *40*, 2234; b) F. Montanarella, K. M. McCall, K. Sakhatskyi, S. Yakunin, P. Trtik, C.

Bernasconi, I. Cherniukh, D. Mannes, M. I. Bodnarchuk, M. Strobl, B. Walfort, M. V. Kovalenko, *ACS Energy Lett.* **2021**, *6*, 4365; c) E. Graham, D. Gooding, J. Gruszko, C. Grant, B. Naranjo, L. Winslow, *J. Instrum.* **2019**, *14*, P11024; d) I. H. B. Braddock, M. Al Sid Cheikh, J. Ghosh, R. E. Mulholland, R. E. J. G. O'Neill, V. Stolojan, C. Crean, S. J. Sweeney, P. J. Sellin, *Nanomater* **2022**, *12*, 2141; e) A. Datta, J. Fiala, S. Motakef, *Sci. Rep.* **2021**, *11*, 22897; f) W. Shen, L. Yang, J. Feng, Y. Chen, W. Wang, J. Zhang, L. Liu, K. Cao, S. Chen, *Inorg. Chem.* **2022**, *61*, 8604; g) S. Kamau, R. G. Rodriguez, Y. Jiang, A. H. Mondragon, S. Varghese, N. Hurley, A. Kaul, J. Cui, Y. Lin, *Micromachines* **2023**, *14*, 1706; h) H. S. Yang, S. H. Noh, E. H. Suh, J. Jung, J. G. Oh, K. H. Lee, J. Jang, *ACS Appl. Mater. Interfaces* **2021**, *13*, 4374.

[26] a) L. Lian, M. Zheng, W. Zhang, L. Yin, X. Du, P. Zhang, X. Zhang, J. Gao, D. Zhang, L. Gao, G. Niu, H. Song, R. Chen, X. Lan, J. Tang, J. Zhang, *Adv. Sci.* **2020**, *7*, 2000195; b) J. Zhou, K. An, P. He, J. Yang, C. Zhou, Y. Luo, W. Kang, W. Hu, P. Feng, M. Zhou, X. Tang, *Adv. Optical Mater.* **2021**, *9*, 2002144; c) B. Wang, P. Li, Y. Zhou, Z. Deng, X. Ouyang, Q. Xu, *ACS Appl. Nano Mater.* **2022**, *5*, 9792; d) K. Li, W. Zhang, L. Niu, Y. Ye, J. Ren, C. Liu, *Adv. Sci.* **2023**, *10*, 2204843; e) J. Luo, X. Wang, S. Li, J. Liu, Y. Guo, G. Niu, L. Yao, Y. Fu, L. Gao, Q. Dong, C. Zhao, M. Leng, F. Ma, W. Liang, L. Wang, S. Jin, J. Han, L. Zhang, J. Etheridge, J. Wang, Y. Yan, E. H. Sargent, J. Tang, *Nature* **2018**, *563*, 541; f) O. Stroyuk, O. Raievska, A. Barabash, C. Kupfer, A. Osvet, V. Dzhagan, D. R. T. Zahn, J. Hauch, C. J. Brabec, *Mater. Adv.* **2022**, *3*, 7894; g) O. Stroyuk, O. Raievska, P. Sebastia-Luna, B. A. H. Huisman, C. Kupfer, A. Barabash, J. Hauch, H. J. Bolink, C. J. Brabec, *ACS Mater. Lett.* **2023**, *5*, 596; h) W. Zhu, W. Ma, Y. Su, Z. Chen, X. Chen, Y. Ma, L. Bai, W. Xiao, T. Liu, H. Zhu, X. Liu, H. Liu, X. Liu, Y. Yang, *Light Sci. Appl.* **2020**, *9*, 112; i) N. Varnakavi, R. Rajavaram, K. Gupta, P.-R. Cha, N. Lee, *Adv. Optical Mater.* **2024**, *12*, 2301868; j) W. Zhou, Y. Yu, P. Han, C. Li, T. Wu, Z. Ding, R. Liu, R. Zhang, C. Luo, H. Li, K. Zhao, K. Han, R. Lu, *Adv. Mater.* **2023**, *36*, 2302140; k) W. Zhou, C. Li, T. Wu, R. Liu, Z. Ding, R. Zhang, Y. Yu, P. Han, R. Lu, *J. Phys. Chem. Lett.* **2023**, *14*, 8577; l) Z. Wang, R. Zhang, X. Mao, D. Zheng, S. Liu, F. Liu, K. Han, B. Yang, *J. Phys. Chem. Lett.* **2022**, *13*, 8613; m) H. Wang, J. Yao, Q. Wei, J. Zhao, B. Zou, R. Zeng, *Adv. Optical Mater.* **2023**, *11*, 2300694; n) W. Zhou, S. Liu, W. Chen, H. Li, S. Yan, J. Yu, C. Liu, L. Zhao, T. Zeng, T. Han, D. Wang, J. Qiu, X. Xu, B. Liu, *Ceram. Intern.* **2022**, *48*, 25086; o) D. Ju, M. Zhou, P. Ran, H. Li, Y. M. Yang, T. Jiang, *ACS Mater. Lett.* **2023**, *5*, 2978; p) B. Aizenshtein, L. Etgar, *Small* **2024**, *20*, 2305755; q) K. Takahashi, M. Arai, M. Koshimizu, Y. Fujimoto, T. Yanagida, K. Asai, *Jpn. J. Appl. Phys.* **2020**, *59*, 072002; r) S. Khalfin, N. Veber, S. Dror, R. Shechter, S. Shaek, S. Levy, Y. Kauffmann, L. Klinger, E. Rabkin, Y. Bekenstein, *Adv. Funct. Mater.* **2022**, *32*, 2110421.

[27] a) X. Liu, Q. Cui, H. Li, S. Wang, Q. Zhang, W. Huang, C. Liu, W. Cai, T. Li, Z. Yang, C. Ma, L. Ren, S. F. Liu, K. Zhao, *ACS Appl. Mater. Interfaces* **2024**, *16*, 16300; b) B. Wang, X. Yang, S. Chen, S. Lu, S. Zhao, Q. Qian, W. Cai, S. Wang, Z. Zang, *iScience* **2022**, *25*, 105593; c) B. Su, G. Zhou, J. Huang, E. Song, A. Nag, Z. Xia, *Laser Photon. Rev.* **2020**, *15*, 2000334.; d) L. Lian, X. Wang, P. Zhang, J. Zhu, X. Zhang, J. Gao, S. Wang, G. Liang, D. Zhang, L. Gao, H. Song, R. Chen, X. Lan, W. Liang, G. Niu, J. Tang, J. Zhang, *J. Phys. Chem. Lett.* **2021**, *12*, 691; e) S. Wang, C. Ma, X. Liu, W. Huang, T. Yang, C. Li, H. Ye, Z. Liu, L. Yin, N. Yuan, J. Ding, L. Chen, K. Zhao, *Adv. Optical Mater.* **2024**, *12*, 2301786.

[28] a) S. Yan, S. Liu, Z. Teng, H. Li, W. Chen, W. Zhou, J. Qiu, X. Yu, S. Wang, X. Xu, *J. Mater. Chem. C* **2022**, *10*, 16294; b) H. Li, Y. Zhang, M. Zhou, H. Ding, L. Zhao, T. Jiang, H. Y. Yang, F. Zhao, W. Chen, Z. Teng, J. Qiu, X. Yu, Y. M. Yang, X. Xu, *ACS Energy Lett.* **2022**, *7*, 2876; c) B. Yang, L. Yin, G. Niu, J.-H. Yuan, K.-H. Xue, Z. Tan, X.-S. Miao, M. Niu, X. Du, H. Song, E. Lifshitz, J. Tang, *Adv. Mater.* **2019**, *31*, 1904711; d) M. Sytnyk, S. Deumel, S. F. Tedde, G. J. Matt, W. Heiss, *Appl. Phys. Lett.* **2019**, *115*, 190501; e) H. Xu, W. Liang, Z. Zhang, C. Cao, W. Yang, H. Zeng, Z. Lin, D. Zhao, G. Zou, *Adv. Mater.* **2023**, *35*, 2300136; f) F. Zhang, Y. Zhou, Z. Chen, X. Niu, H. Wang, M. Jia, J. Xiao, X. Chen, D. Wu, X. Li, Z. Shi, C. Shan, *Laser Photon. Rev.* **2023**, *17*, 2200848; g) W. Gao, G. Niu, L. Yin, B. Yang, J.-H. Yuan, D. Zhang, K.-H. Xue, X. Miao, Q. Hu, X. Du, J. Tang, *ACS Appl. Electron. Mater.* **2020**, *2*, 2242; h) D. Liang, X. Liu, B. Luo, Q. Qian, W. Cai, S. Zhao, J. Chen, Z. Zang, *EcoMat.* **2023**, *5*, e12296; i) N. K. Nandha, A. Nag, *Chem. Commun.* **2018**, *54*, 5205; j) T.-C. Wang, S.-Y. Yao, S.-P. Yan, J. Yu, Z.-Y. Deng, A. N. Yakovlev, B. Meng, J.-B. Qiu, X.-H. Xu, *ACS Appl. Mater. Interfaces* **2023**, *15*, 23421; k) N. Li, Z. Xu, Y. Xiao, Y. Liu, Z. Yang, S. Liu, *Adv. Optical Mater.* **2022**, *10*, 2102232.

[29] a) J. Cao, Z. Guo, S. Zhu, Y. Fu, H. Zhang, Q. Wang, Z. Gu, *ACS Appl. Mater. Interfaces* **2020**, *12*, 19797; b) B. Su, J. Jin, K. Han, Z. Xia, *Adv. Funct. Mater.* **2023**, *33*, 2210735; c) J. Li, J. Wang, Y. Zhang, H. Wang, G. Lin, X. Xiong, W. Zhou, H. Luo, D. Li, *2D Mater.* **2018**, *5*, 021001.

[30] Directive 2011/65/EU of the European Parliament and of the Council of 8 June 2011 *Off. J. Europ. Union.* **2011**, *54*, 88.

[31] a) L. Zhang, X. Wang, X. Wang, X. Wang, Y. Luo, C. Tan, L. Jiang, Y. Wang, W. Liu, *Inorg. Chem.* **2023**, *62*, 6421; b) Y.-H. Liu, N.-N. Wang, M.-P. Ren, X. Yan, Y.-F. Wu, C.-Y. Yue, X.-W. Lei, *ACS Appl. Mater. Interfaces* **2023**, *15*, 20219; c) Y. Xu, A. Ying, J. Peng, F. Yao, R. Li, Y. Tan, S. Gong, Q. Lin, *Sci. Chin. Mater.* **2023**, *66*, 724; d) R.-W. Huang, X. Song, S. Chen, J. Yin, P. Maity, J. Wang, B. Shao, H. Zhu, C. Dong, P. Yuan, T. Ahmad, O. F. Mohammed, O. M. Bakr, *J. Am. Chem. Soc.* **2023**, *145*, 13816; e) N. Yawai, W. Chewpraditkul, C. Wanarak, M. Nikl, W. Ratanatongchai, *Optical Mater.* **2014**, *36*, 2030; f) Y. Wang, M. Li, Z. Chai, Y. Wang, S. Wang, *Angew. Chem., Int. Ed.* **2023**, *62*, e202304638.

Olexiy Balitskii has been a VW Scholar for Solution-Processed Semiconductor Materials Group at the Friedrich-Alexander Universität Erlangen-Nürnberg, Germany, since 2022. Before, he worked at the Ivan Franko National University of Lviv, securing several post-doc positions at the University of California as a Fulbright Scholar, Johannes Kepler Universität Linz, Universities of Gothenburg, and Fribourg. His research objectives are the fabrication and properties of layered 2D semiconductors and colloidal nanocrystals applicable in electronics, energy conversion, and biotechnology.

Wolfgang Heiss has been an associate professor for Solution-Processed Semiconductor Materials at the Friedrich-Alexander Universität Erlangen-Nürnberg, Germany, since 2014. Before that, he was working at the Johannes Kepler Universität Linz and at the University of Technology in Vienna, both in Austria. While the research of Prof Heiss was devoted to semiconductor physics and devices for his career, his most successful research is related to the demonstration of solution-processed perovskites for X-ray detection. In this field, he demonstrated the first solution-processed X-ray detector ever and contributed to the success of polycrystalline perovskite wafers for X-ray detection and imaging.